Environmental Earth Sciences (2026) 85:404
https://doi.org/10.1007/s12665-026-13141-7

ORIGINAL ARTICLE

Thermo-hydro-mechanical response of the operation style in a faulted Malm reservoir: Storage triplet vs. hydrothermal doublet

Ali Dashti[1] · Kai Stricker[2] · Thorsten Hörbrand[2] · Rahim Habibi[1] · Kilian Beichel[2] · Thomas Kohl[1]

Received: 16 June 2026 / Accepted: 9 September 2026

Abstract

The existing heat in the earth can be considered as an abundant source of clean energy. Geothermal applications have extracted this resource via various approaches, such as petro- and hydrothermal systems or heat pumps. In recent years, thermal energy storage systems (ATES), which balance the temporal mismatch of the energy demand and supply were widely developed, primarily in the Netherlands. Herein we compared the fully elastic thermo-hydro-mechanical response of two different geothermal systems: a hydrothermal doublet and a high-temperature (HT) ATES triplet, both located in the karstified and faulted Malm aquifer in the north of Munich (south of Germany). Both systems have a negligible impact on the pressure field of the Malm reservoir due to its high permeability. The geomechanical responses at the scale of the reservoir are primarily governed by thermoelasticity, with only minor poroelastic effects due to low pressure variations. In our linear elastic constitutive framework, the cyclic injection and production of the HT-ATES triplet lead to slightly lower stress-field perturbations than the continuous operation of the hydrothermal doublet under the investigated operating conditions. As a result, lower fault destabilization and smaller induced displacements were computed in the HT-ATES scenario. These differences are attributed to the cyclic thermal loading and reduced cumulative thermal perturbation associated with the storage operation. Additionally, the heterogeneity of the reservoir, represented by differences in the permeability of the layers, has a notable impact on both thermal recovery and the fault stability in the HT-ATES triplet.

Keywords Aquifer thermal energy storage (ATES) · Hydrothermal doublet · Thermo-hydro-mechanical simulations · Malm

Nomenclature

ATES	Aquifer thermal energy storage
HT-ATES	High-temperature aquifer thermal energy storage
THM	Thermo-hydro-mechanical
m	Fluid mass
v_S	Velocity of the solid skeleton
F	Flux
q	Source term
v	Darcy velocity
P	Pore pressure
k	Permeability tensor
η	Fluid dynamic viscosity
ρ	Fluid density
g	The gravitational acceleration
e	Heat energy
F^T	Heat fluid flux
q^T	Heat source
h	Specific enthalpy of phase
λ	Thermal conductivity tensor
σ_{ij}^{eff}	The effective stress tensor
σ_{ij}^{eff}	Total stress tensor
α	Biot coefficient
δ_{ij}	Kronecker delta tensor
E_{ijkl}	Elasticity tensor of the solid skeleton (drained version)
ε_{kl}	Infinitesimal strain tensor
ε_{kl}^{el}	Elastic strain tensor
ε_{kl}^{th}	Thermal strain tensor
α_T	Linear drained thermal expansion coefficient

✉ Ali Dashti
Ali.dashti@kit.edu

[1] Institute of Applied Geosciences, Karlsruhe Institute of Technology (KIT), Karlsruhe, Germany

[2] SWM Services GmbH, Emmy-Noether-Strasse 2, 80992 Munich, Germany

Published online: 17 September 2026

T	Temperature
ΔT	Temperature change
u	Displacement vector
$t_i/\boldsymbol{t}^{eff}$	Effective traction vector
$n_j/\boldsymbol{n}$	Unit normal vector
σ_N^{eff}	Effective normal stress
τ	Shear stress
ST	Normalized slip tendency
C	Cohesion value
μ	Friction coefficient
Well H	Hot well in HT-ATES triple
Well C	Cold well in HT-ATES triple
Well B	Buffer well in HT-ATES triple
Well P	Production well in hydrothermal doublet
Well I	Injection well in hydrothermal doublet
Homo.	Homogeneous
Extr.het.	Extremely heterogeneous
Mod.het.	Moderately heterogeneous
BC	Boundary condition
IC	Initial condition
S_H	Maximum horizontal stress
S_h	Minimum horizontal stress
S_v	Vertical stress
LOT	Leak-off test
P	Pressure
EOS	Equation of State
$T(z)$	Temperature as a function of depth
$T_{surface}$	Temperature at the surface
z	Depth
GT	Geothermal gradient
$T_{surface}$	Temperature at the surface
$P(z)$	Pressure as a function of depth
z_0	Depth of the water table
ϵ	Thermal recovery efficiency
$T_{out}(t)$	Produced temperature form Well H over time
T_{res}	Reservoir temperature
$T_{in}(t)$	Injected temperature over summer period
DAS	Distributed acoustic sensing

Introduction

With the increasing global demand for energy and the corresponding rise in greenhouse gas emissions, efficient and reliable renewable energy generation is essential for a sustainable future (Jacobson et al. 2017; Hassan et al. 2024; Solangi and Magazzino 2025). Geothermal systems are a significant resource for abundant clean energy (Barbier 2002; Chamorro et al. 2012). Energy production from hydrothermal systems (Moeck 2014) and storage applications (Lee 2010) are both proven to enable CO_2-free power/heat generation. The South German Molasse Basin stands out as a premier region for geothermal power generation utilizing hydrothermal resources (Cröniger et al. 2022). This prominence is largely due to the highly productive Upper Jurassic Malm aquifer, which serves as a key target for deep, > 1.2 km, geothermal applications (Wadas et al. 2023). These units, reaching thicknesses of up to 600 m, comprise limestones and dolomites. These carbonate sediments exhibit facies variations and have undergone multiphase karstification (Wolfgramm et al. 2007) making the reservoir hydraulics primarily controlled by the karst network (Quinn et al. 2006; Hörbrand et al. 2025). The lithospheric bending caused by the Alpine Orogeny further influenced the reservoir's characteristics, promoting extensive normal faulting (Wolfgramm et al. 2007; Mraz 2019). The aforementioned factors exert a significant influence on the spatial distribution of hydraulic properties within the Malm aquifer (Konrad et al. 2021; Fadel et al. 2022; Hörbrand et al. 2025).

One geothermal project within the Molasse Basin experienced a premature thermal breakthrough, jeopardizing the long-term sustainability of heat extraction (Fadel et al. 2022). Such thermal breakthroughs are mainly caused by challenges associated with cold water plume migration from the injection well into the reservoir. The continuous injection of cold water creates a progressively expanding cold front, potentially reaching the production well and compromising system efficiency (Li et al. 2016). Although sensitivity analyses can assess the impact of individual parameters—such as reservoir geometry, flow rate, well spacing, and permeability—on overall performance, accurately predicting thermal breakthroughs remains a complex task that necessitates extensive numerical modelling (Kong et al. 2017; Aliyu and Chen 2017; Shi et al. 2023).

Integrating an aquifer thermal energy storage (ATES) concept into existing hydrothermal doublets within the Molasse Basin presents a promising optimization strategy to enhance system performance and reduce operational risks. While existing normal faults in the Molasse Basin can significantly accelerate thermal breakthroughs in hydrothermal doublets (Jahanbakhsh et al. 2016), their impact on ATES schemes is comparatively less relevant (Dashti et al. 2024). The high-temperature, c. 40 °C higher than the ambient temperature (Heldt et al. 2023), HT-ATES concept leverages the Malm aquifer to store surplus heat generated during summer months, effectively bridging the temporal mismatch between geothermal production and district heating demand (Dickinson et al. 2009; Wang et al. 2024). HT-ATES shows long-term reliability, with properly maintained systems delivering stable heating for decades (Bloemendal et al. 2014; Fleuchaus et al. 2018; Mahon et al. 2022; Shah et al. 2024). These benefits make HT-ATES an attractive and sustainable solution for district heating and cooling in municipalities such as Munich, Germany.

Figure 1 shows the conceptual difference between the HT-ATES triplet and hydrothermal doublet. In the HT-ATES triplet, three wells are used: a bidirectional hot well, which injects hot fluid into the reservoir during summer and produces it during winter; a cold well, which reinjects the cooled fluid (produced from the hot well) into the reservoir; and a buffer well, which produces ambient-temperature reservoir fluid. The concept behind triplets is well documented by Bloemendal et al. (2022), van Esch et al. (2025), and Hörbrand et al. (2023). In the hydrothermal doublet, only two wells are used: a production well, which continuously produces ambient-temperature reservoir fluid, and an injection well, which continuously reinjects the same fluid after heat extraction. Because the doublet operates continuously in a single direction at each well, rather than cyclically as in the triplet, it induces a larger cumulative thermal perturbation around the wells, as illustrated schematically in Fig. 1.

A crucial challenge in HT-ATES engineering is the dynamic response of the underground media, since thermally and hydraulically induced stress changes can affect both the operational performance of the system leading to thermal breakthrough and the mechanical stability of pre-existing faults, raising the possibility of induced seismicity (Wesselink et al. 2018). Thermal changes induced by the operations alter the mechanical properties of the rock, while the hydraulic behaviour also undergoes a complex interplay with these human-induced (thermal and mechanical) modifications (Lei et al. 2021). Therefore, a comprehensive understanding of the thermo-hydro-mechanical (THM) processes is essential (Ghassemi 2012; Parisio et al. 2019; Stober et al. 2023; Vaezi et al. 2025). However, quantifying THM processes in geothermal applications presents a significant scientific challenge (Zareidarmiyan et al. 2020; Jin et al. 2022). The inherent complexity arises from the strong inter-dependencies between thermal transport, fluid flow, and deformation of the rock matrix. Analytical solutions for THM problems are often scarce or nonexistent, and replicating the complex interactions (within the reservoir) through experimentation proves equally challenging (Cui and Wong 2022). Compounding these challenges are the prohibitive costs and extensive time requirements associated with experimental investigations (Pandey et al. 2018). These limitations (time, safety, technical constraints, cost, etc.) render numerical modelling as a more practical approach for exploring THM coupling effects (Habibi et al. 2023). However, developing robust THM models for subsurface simulations also remains highly challenging due to the complexities of multiphysics interactions and the presence of discontinuities e.g., fractures or karst.

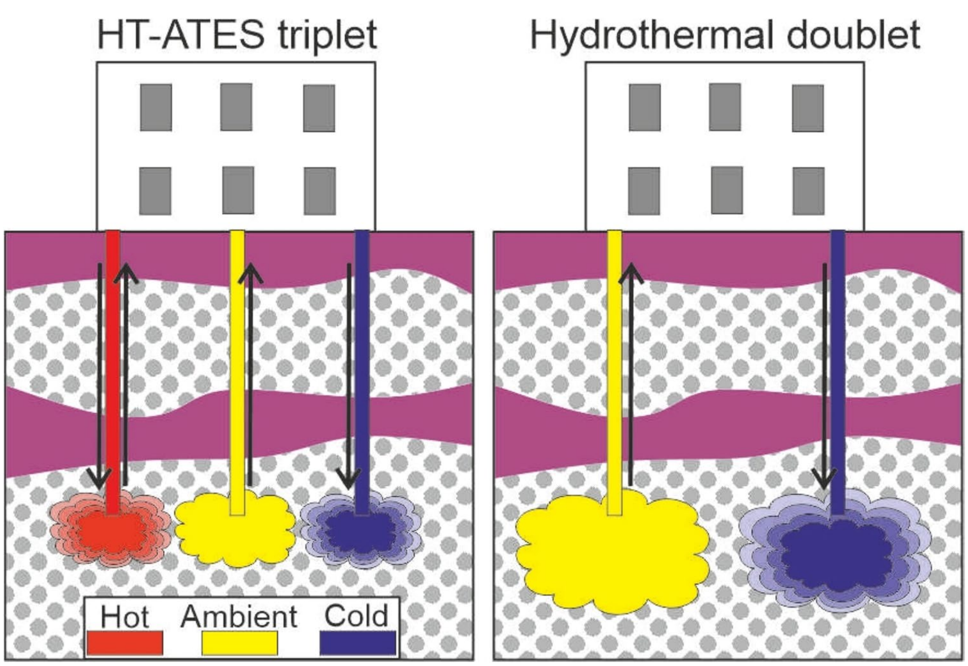

Fig. 1 Schematic comparison of the operational principles of the HT-ATES/storage triplet and the classic hydrothermal doublet. Red and blue indicate the thermal perturbation induced by injecting hot and cold water, respectively; yellow indicates reservoir fluid at ambient temperature. In the triplet, the hot well operates bidirectionally (arrows in both directions), injecting hot fluid in summer and producing it in winter. The cold well operates unidirectionally, reinjecting the cooled fluid produced by the hot well. The buffer well produces ambient-temperature reservoir fluid to maintain mass balance. In the doublet, the production well continuously produces ambient-temperature fluid, while the injection well continuously reinjects the cooled fluid after heat extraction. The induced thermal plumes are shown schematically and not to scale; the larger plumes around the doublet's wells reflect its continuous, single-direction operation, in contrast to the cyclic operation of the triplet.Adopted from Bloemendal et al. (2022) and Hörbrand et al. (2023)

The present study adopts a THM framework based on single-phase, fully saturated flow coupled with linear elastic mechanics. This framework is appropriate for a first comparative assessment of the relative geomechanical response of the two operational schemes. Coupled THM modelling of geothermal reservoirs, thermally induced stress perturbations, and slip-tendency analysis are all individually well established. However, a direct comparison of their geomechanical response, specifically the fault stability, between a hydrothermal doublet and an HT-ATES triplet in the faulted Malm reservoir has not yet been addressed. This comparison matters because the two schemes differ in their thermal loading pattern: continuous for the doublet, cyclic for the triplet. Yet their relative impact on fault stability in the Malm reservoir has not been systematically quantified. This study addresses that gap through a suite of THM simulations. We aim to enhance the understanding of THM processes in the context of different geothermal applications (hydrothermal doublet and HT-ATES triplet), with a particular focus on the influence of uncertainties in the permeability distribution within the reservoir. Using a common geological framework representative of the faulted Malm aquifer near Munich, we evaluate whether the HT-ATES triplet poses a lower risk of fault destabilization than the conventional hydrothermal doublet. We first compare the two schemes under a homogeneous reservoir assumption. We then extend the analysis to two simplified heterogeneity scenarios, since karstification as a well-documented feature of the Malm reservoir can strongly influence the THM response of the system. This allows to assess how such heterogeneity affects both the heat recovery and fault stability, beyond what the homogeneous case alone can capture.

Methodology

This study uses the open-source finite element simulator PorousFlow within the MOOSE framework (Wilkins et al. 2021; Lindsay et al. 2022). The PorousFlow module enables fully coupled THM simulations. Of these capabilities, the present study activates only fully saturated, single-phase, single-component fluid flow, coupled with heat transport and linear elastic mechanics. Permeability evolution, multiphase behaviour, and multicomponent transport are not activated in the present model. At the modelled depths (1470–2000 m), the hydrostatic pressure substantially exceeds the saturation pressure of water at the maximum simulated temperature (140 °C, for which the saturation pressure is c. 0.36 MPa (Wagner and Pruß 2002)). The fluid therefore remains well within the liquid stability field throughout the domain, and boiling, flashing, or vapour-phase formation are not expected to occur, even locally near the injection wells. The relevant equations for the THM simulations of this study are described in detail below.

Fluid flow

To solve the hydraulic field in a THM simulation, PorousFlow uses mass conservation that is described by the continuity equation as already elaborated by Wilkins et al. (2021):

$$\frac{\partial m}{\partial t} + m\nabla \cdot \upsilon_S + \nabla \cdot F - q = 0 \tag{1}$$

where m is the fluid mass, υ_S is the velocity of the solid skeleton, F represents the flux, and q is the source term. The coupling to the solid mechanics in PorousFlow is done via the $m\nabla \cdot \upsilon_S$ part of the equation. The changes in porosity and permeability of the solid skeleton (through stress or strain changes) also facilitate the coupling. In this study permeability is held constant while porosity is updated at each time step. PorousFlow can handle multi-phase and multicomponent flow (Wilkins et al. 2021), however we assumed that the pore space is fully saturated with a single fluid component (water) for the sake of simplicity. Consequently, only advective transport of fluid mass is considered, while molecular diffusion and mechanical dispersion are neglected because no dissolved species are simulated. The general mass flux may be expressed as

$$F = F_{advection} + F_{diffusion+dispersion} \tag{2}$$

where the second term ($F_{diffusion+dispersion}$) represents molecular diffusion and mechanical dispersion. Since the present study considers a fully saturated single-component fluid without solute transport, this contribution is neglected, and the mass flux reduces to Darcy advection:

$$F_{advection} = \rho \upsilon = -\rho \frac{k}{\eta}(\nabla P + \rho g) \tag{3}$$

where υ is the Darcy velocity, P is the pressure of each specific phase (one fully saturating phase in our case), k is the permeability tensor, η is the fluid dynamic viscosity, ρ represents fluid density, and g is the gravitational acceleration vector.

Heat flow

PorousFlow assumes a local thermodynamic equilibrium for the liquids and solid phases. Heat transport is represented separately through fluid advection and thermal conduction. The energy conservation for heat is described by the continuity equation:

$$\frac{\partial e}{\partial t} + e\nabla \cdot v_S + \nabla \cdot F^T - q^T = 0 \tag{4}$$

where e is heat energy, F^T represents the heat fluid flux, and q^T is a heat source. Rock grain density, the specific heat capacity of the rock, and the internal energy of the fluid phase are used to calculate the heat energy (e). The $e\nabla \cdot v_S$ term of the equation, and changes in porosity and permeability of the solid skeleton enable the coupling to solid mechanics. PorousFlow generally supports coupling between solid mechanics and flow through stress- or strain-dependent porosity and permeability formulations. In the present study, porosity is actively updated as a function of stress and strain during the simulations, while permeability is held constant throughout. The mechanical-to-hydraulic coupling therefore occurs through two channels: the $m\nabla \cdot v_S$ term in Eq. 1 and the resulting porosity changes. The changes in porosity affect the fluid and heat energy storage terms (Eq. 1 and 4) without altering permeability.

The heat flux is a sum of heat conduction and convection with the fluid:

$$F^T = -\lambda \nabla T + hF_{advection} \tag{5}$$

where h is the specific enthalpy of phase (water in our single-phase assumption) and λ is the thermal conductivity tensor, which in PorousFlow is a function of the thermal conductivities of the fluid and rock phases.

Solid mechanics

PorousFlow leverages the available functionalities from other MOOSE modules in order to handle solid mechanics and the coupling with fluid and heat flow. The evolution of porosity with pressure, strain, and temperature is fundamental to the coupling between flows and solid mechanics. The effective stress tensor is calculated as

$$\sigma_{ij}^{eff} = \sigma_{ij}^{tot} + \alpha \delta_{ij} P \tag{6}$$

where σ_{ij}^{eff} represents the effective stress tensor, σ_{ij}^{tot} is the total stress tensor, α is the Biot coefficient, and δ_{ij} is the Kronecker delta tensor. Then, the elastic constitutive law (McTigue 1986) links the deformation of the porous solid to the effective stress tensor:

$$\varepsilon_{kl}^{el} = \varepsilon_{kl} - \varepsilon_{kl}^{th} \tag{7}$$

$$\varepsilon_{kl}^{th} = \delta_{kl} \alpha_T \Delta T \tag{8}$$

$$\sigma_{ij}^{eff} = E_{ijkl}(\varepsilon_{kl} - \varepsilon_{kl}^{th}) \tag{9}$$

where ε_{kl}^{el} is the elastic strain tensor, ε_{kl} is the total strain tensor, ε_{kl}^{th} represents the isotropic thermal strain, α_T is the linear drained thermal expansion coefficient, ΔT is the temperature change defined as $T - T_{reference}$, and E_{ijkl} is the elasticity tensor of the solid skeleton (drained version), which is inverse of the drained compliance tensor. The infinitesimal strain tensor is composed of the displacement vector (u):

$$\varepsilon_{kl} = \frac{1}{2}\left(\frac{\partial u_k}{\partial x_l} + \frac{\partial u_l}{\partial x_k}\right) \tag{10}$$

The total infinitesimal strain tensor is obtained from the displacement vector as given in Eq. 10. For the adopted linear thermoelastic formulation, the elastic strain is obtained by subtracting the isotropic thermal strain from the total strain as presented in Eq. 7.

All nine stress components and unit normal vectors to each face of the mesh are calculated as auxiliary variables in PorousFlow. Based on Cauchy's law, the effective traction vector (t_i^{eff} or $\boldsymbol{t}^{eff}$) acting on a surface can be calculated based on the effective stress tensor and unit normal vector (n_j or $\boldsymbol{n}$) (Zoback 2007):

$$\boldsymbol{t}^{eff} = \boldsymbol{\sigma}^{\boldsymbol{eff}} \bullet \boldsymbol{n}, \text{i.e.}, t_i^{eff} = \sigma_{ij}^{eff} n_j \tag{11}$$

which in a matrix form is

$$\begin{bmatrix} t_1^{eff} \\ t_2^{eff} \\ t_3^{eff} \end{bmatrix} = \begin{bmatrix} \sigma_{11}^{eff} & \sigma_{12}^{eff} & \sigma_{13}^{eff} \\ \sigma_{12}^{eff} & \sigma_{22}^{eff} & \sigma_{23}^{eff} \\ \sigma_{13}^{eff} & \sigma_{23}^{eff} & \sigma_{33}^{eff} \end{bmatrix} \bullet \begin{bmatrix} n_1 \\ n_2 \\ n_3 \end{bmatrix} \tag{12}$$

Then, the effective normal stress acting on the normal surface (σ_N^{eff}) can be calculated as the dot product of the traction vector and unit normal vector:

$$\sigma_N^{eff} = n_i \sigma_{ij}^{eff} n_j \tag{13}$$

which in a matrix form will be

$$\sigma_N^{eff} = \begin{bmatrix} n_1 \\ n_2 \\ n_3 \end{bmatrix} \bullet \begin{bmatrix} \sigma_{11}^{eff} & \sigma_{12}^{eff} & \sigma_{13}^{eff} \\ \sigma_{12}^{eff} & \sigma_{22}^{eff} & \sigma_{23}^{eff} \\ \sigma_{13}^{eff} & \sigma_{23}^{eff} & \sigma_{33}^{eff} \end{bmatrix} \bullet \begin{bmatrix} n_1 \\ n_2 \\ n_3 \end{bmatrix} \tag{14}$$

The following equation also gives the magnitude of the shear stress (τ) acting on each surface:

$$\tau = \sqrt{(t_i^{eff} t_i^{eff}) - (\sigma_N^{eff})^2} \tag{15}$$

The governing equations above constitute a coupled THM formulation in the specific sense that changes in temperature, pressure, and stress/strain are solved simultaneously and influence one another within each timestep. This should be distinguished from more general THM frameworks that additionally incorporate multiphase or multicomponent flow, permeability and porosity evolution, or inelastic mechanical behaviour (e.g., plasticity, damage, fracture propagation). The present study adopts a saturated, single-phase thermo-poroelastic formulation with linear elastic mechanical behaviour, which we consider appropriate for the comparative assessment presented here but which does not capture the additional processes listed above.

In this study, the ratio between the shear and effective normal stress is used to define the normalized slip tendency (ST) value as

$$ST = \frac{\tau}{\mu\sigma_N^{eff} + C} \tag{16}$$

where μ is the friction coefficient and C is the cohesion value and is considered to be 0 in this study (conservative approach). Accordingly, the effective normal stress and shear stress are derived directly from the effective traction vector. The pore-pressure contribution is already incorporated in the effective stress according to the adopted Biot effective-stress formulation and is therefore not applied separately in the fault-stability calculation. ST values equal to or greater than the cut-off (1.0) indicate exceeding the friction (slip) criterion. Although Earth and atmospheric tides can induce measurable subsurface strain (Zhang et al. 2019), these effects are not considered in this study, as their magnitude is minor relative to the operation-induced thermo-hydro-mechanical perturbations at the investigated depth range.

Model description

A 3-D synthetic geological model inspired by the northern Munich Malm reservoir in the Molasse Basin forms the core of the numerical study. While this model is designed to represent the reservoir in the northern part of Munich, it does not correspond to a specific site. In this region, the geothermal gradient is assumed to be 35 K km^{-1} giving the Malm reservoir a temperature of 80–85 °C. This allows for a high temperature difference during storage (55–60 °C when injecting at 140 °C), which is important for thermal recovery. Furthermore, the connection to district heating networks and a high-temperature heat source are available in this region (Hörbrand et al. 2023). The top of the Malm reservoir in the area of interest is 1470 m below the mean sea level. As the area of interest is not covered by seismic data, we constructed a synthetic structural model by using a real fault, which is part of the "Markt-Schwabener-Verwurf" and was interpreted from the GRAME seismic cube. The GRAME project involved the acquisition of an extensive 3-D seismic survey across southern Munich in 2015/2016, representing one of the largest urban geothermal seismic campaigns conducted in Europe. This seismic exploration covered an area of approximately 170 km^2 in the southern part of the city and was specifically designed to image the deep hydrothermal reservoir hosted within the Upper Jurassic (Malm) carbonate formations at depths of around 3 km. The resulting high-quality seismic dataset formed the basis for an updated 3-D geological model of the Munich subsurface, improving the understanding of reservoir architecture, faults, and potential fluid pathways, and significantly reducing exploration uncertainty (Bruss et al. 2018).

Based on this structural framework, we introduced a normal fault with varying dip angles and strikes into the model developed in this study. From a hydraulic perspective, since systematic evidence does not indicate enhanced permeability along faults in the Malm aquifer (Hörbrand et al. 2025), we implemented the fault with neutral permeability. As this study lacks site-specific data on transmissivity within the fault core or damage zone, the conclusions of Hörbrand et al. (2025) on the fault permeability are adopted as ground truth. The hydraulic impact of the fault is instead represented by juxtaposing layers of differing permeability across the fault plane.

To generate the complex fault surface in the mesh (Fig. 2a and b), the new surface fitting functionality of the Gmsh software (Geuzaine and Remacle 2009; Dashti et al. 2023) is used in this study. The fault geometry and offset are calculated in the geological model. Then, a grid of points representing the fault surface is imported into Gmsh to reconstruct and mesh it. The unstructured mesh of the model is composed of tetrahedral elements. In the mesh, the element size gradually increases from 2 m around the wells to 600 m at the boundaries of the model. The fault surface is also refined due to its importance in the THM simulations. In total, the model contains 104′591 nodes and 470′882 elements.

The lateral extension of the model is large enough (18 km × 16 km) to avoid possible boundary effects. Vertically, the model extends over 4 km with three main units: the cap rock, six reservoir layers, and the basement (Fig. 2a). The topmost reservoir layer is assumed to be 30 m thick while the other 5 layers have a fixed 100 m thickness, resulting in a Malm reservoir with a thickness of 530 m. The chosen thicknesses for the confining cap rock and basement ensure that the results are independent of the top and bottom boundaries. Two different applications, i.e. exploitation schemes, are developed in this study: a classic hydrothermal doublet and a triplet HT-ATES system. These two

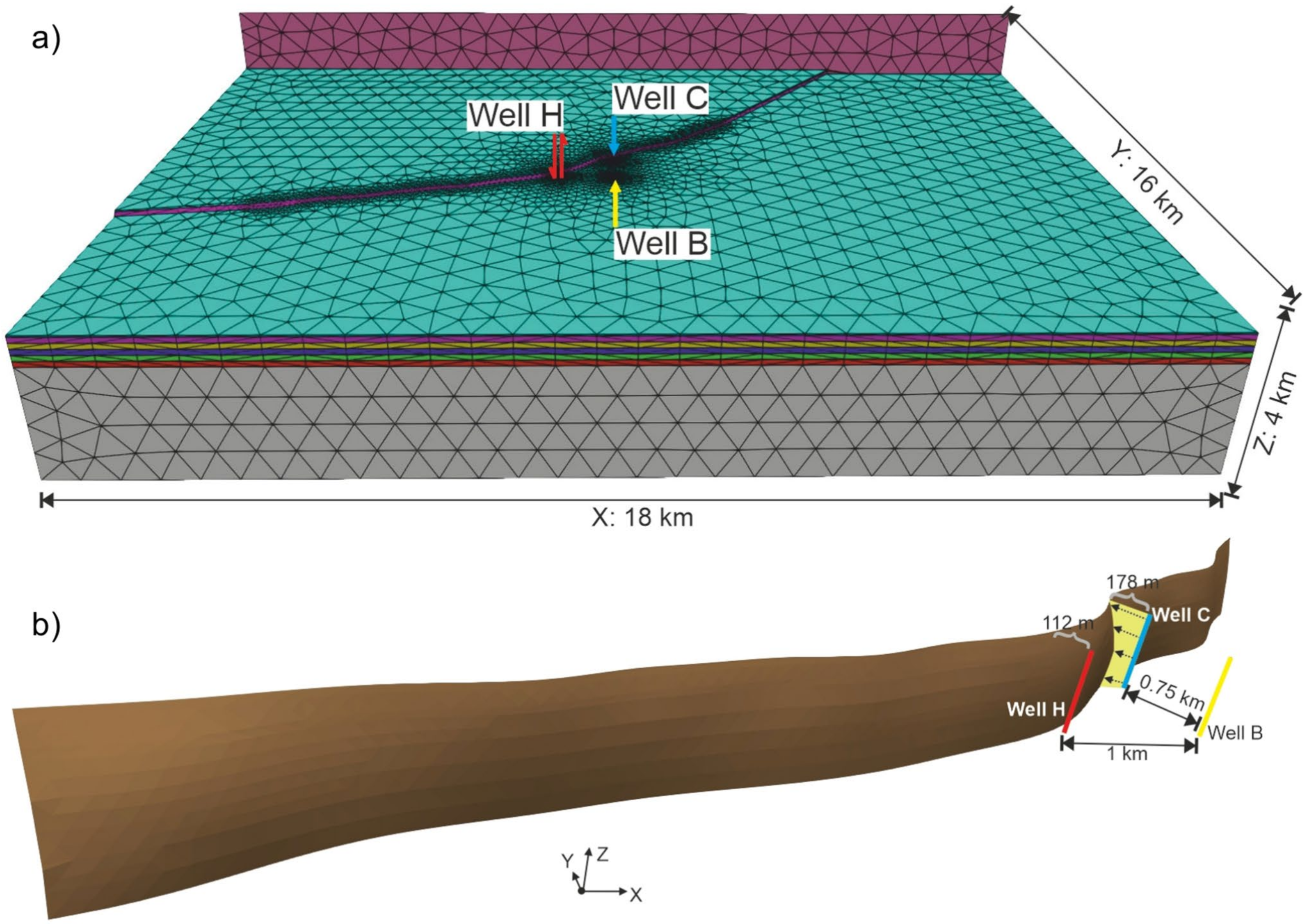

Fig. 2 **a**) The 3-D mesh generated for the simulations in the Molasse basin. The cap rock is not shown to have a better view of the designed triplet. The location of the Well H is highlighted by red arrows in the middle of the model. The yellow upward arrow shows the location of the Well B. The blue downward arrow denotes the location of the Well C. For the hydrothermal doublet only Well P and Well I are active, which are placed exactly at the location of the Well H and Well C, respectively. **b**) A closer view into the implemented normal fault with changing dipping angle and orientation. The complexity of the fault surface results in the variation of fault-well distances highlighted by a yellow patch and arrows making an orthogonal connection between Well C to the fault surface. The orthogonal distance between top of the Well C and fault surface is 178 m, while it decreases in the middle part reservoir. The orthogonal distance between top of the Well H and fault surface is 112 m and variates along the reservoir

operational setups are compared in terms of their potential impact on the fault stability over a 10-year simulation period.

For our HT-ATES application, three vertical wells are positioned in close proximity to the fault (Fig. 2). In this triplet setting there is one hot well ("Well H"), one cold well ("Well C"), and one buffer well ("Well B"). Well H is bidirectional, injecting hot fluid at 140 °C during the 6-month 'summer period' and producing fluid during the following 6-month 'winter period'. Well C operates unidirectionally, injecting fluid at 50 °C only during the winter period. The hot water temperature, 140 °C, is selected based on the heat provided from the steam district heating network of Munich. Chosen cold water temperature, 50 °C, is the minimum reinjection temperature based on the requirements of the hot water district heating network. During the hot fluid injection phase in Well H (summer), the unidirectional Well B is used to produce reservoir fluid to maintain mass balance within the model. As elaborated by Hörbrand et al. (2023), the triplet layout with the third well, Well B, brings thermal and chemical benefits. Well B in the summer period produces the ambient fluid from the reservoir (with a temperature of 80–85 °C), which should be heated to 140 °C before being injected into the Well H. In this sense, the triplet can be understood as an "enhanced geothermal doublet," producing both geothermal and stored thermal energy. Well C is therefore not made bi-directional, since its role is receiving cooled water during winter period. A chemical benefit applies when CO_2 is used for scale inhibition: unlike a doublet, where progressively hardened water is reproduced each cycle and demands an ever-increasing CO_2 dose, the triplet ensures Well H always receives fresh heated water each period produced from Well B (see Hörbrand et al. (2023) for more details). To implement the injection and production of heat and mass in the model, the Dirac Kernel in PorousFlow is applied at mesh nodes. In our PorousFlow implementation, each well is represented by a series of Dirac point sources distributed along the entire 530 m reservoir interval, with a spacing of 1 m between adjacent points. Consequently, mass and thermal energy are injected into or extracted from the reservoir along the full length of the well represented by 530 points. The MOOSE control system is used to dynamically update the operational mode of the bidirectional well. In this setup, the flow rate for both injection and production is set at 150 l s^{-1}. The simulation covers a 10-year period, divided into 20 alternating six-month summer and winter periods. During the summer period, hot water is injected into Well H; during the winter period, Well H is switched to production mode. The simulation begins with a summer period (0.0 to 0.5 year) and ends with a winter period (9.5 to 10.0 years). MOOSE allows for gradual time-step increases within each period, with the step size ranging from 1 h to 10 days. This method ensures better numerical convergence when the operational mode of the well transitions.

In the classic hydrothermal doublet, two wells are positioned within the model. The design of these wells is similar to the HT-ATES triplet, but without Well C. All the wells are embedded within the 530 m thick Malm reservoir. In this configuration, one well is designated as the production well ("Well P"), which continuously produces fluid, while the other is the injection well ("Well I"), injecting cold fluid at 50 °C. Well P can be considered as an alias for Well H but with a different operational mode. While Well H injects hot (140 °C) fluid for 6 months and is in production mode within the next 6-month period, Well P continuously produces the ambient reservoir fluid. Well I is located at the same position as Well C but with a continuous injection pattern rather than a cyclic one. Both wells have an injection/production flow rate of 150 l s^{-1}. The simulation duration for the hydrothermal doublet is also set to 10 years, with a time-stepping similar to the HT-ATES simulation. The hydrothermal doublet and the HT-ATES triplet serve different engineering objectives and follow different thermal loading histories. This distinction should be considered when interpreting the comparative results.

For both the HT-ATES and hydrothermal applications the fluid flow is modeled using temperature- and pressure-dependent properties of water based on the IAPWS-IF97 formulation (Cooper and Dooley 2007). Specifically, the Water97FluidProperties model is employed, which is based on an Equation of State (EOS) for water to consistently describe its thermophysical properties. This approach enables accurate evaluation of key fluid properties, including density, viscosity, and enthalpy, over the range of pressures and temperatures relevant to geothermal reservoir conditions. The use of this EOS ensures a realistic representation of fluid behavior in the coupled thermo-hydro-mechanical simulations.

For both applications, the initial condition (IC) and boundary condition (BC) strategies are the same. Depth-dependent functions are defined to set the initial conditions for pressure and temperature:

$$T(z) = T_{surface} + z \times \mathrm{G}T \quad (17)$$

where T is the temperature, z denotes the depth and GT the geothermal gradient assumed to be 35 K km^{-1} in this study. For the pressure, the IC is calculated based on the following function (assuming a hydrostatic equilibrium):

$$P(z) = (z - z_0) \times \rho \times g \quad (18)$$

where z_0 represents the depth of the water table (c. 10 m for the Molasse basin), ρ is the density of the fluid and g denotes the gravitational acceleration.

The displacement values in three directions are set to 0 at the initial condition. To reach the equilibrium, simulations are run for 1 year without any production and injection.

The same depth-dependent temperature and pressure functions are applied as BC for both variables. The pressure BC is set on the four side faces of the model, while the temperature BC is applied on six faces, excluding the top and bottom surface of the model. With this approach, MOOSE a depth-dependent function to calculate the temperature BC at the six faces of the model. The displacement and stress BCs are set based on the stress regime in the Molasse Basin which is fully elaborated by Ziegler and Heidbach (2020). A strike-slip regime with 0° N (Reinecker et al. 2010; Ziegler and Heidbach 2020) as the direction of the maximum horizontal stress (S_H) is chosen in this study. Therefore, the maximum amount of stress acts on the y direction while in the z and x directions, the medium (S_V) and minimum (S_h) stress are set, respectively. For a rock density of 2′300 kg m^{-3}, the S_V gradient is set to 22.6 kPa m^{-1}. The S_h value in this study comes from the formation integrity and leak-off tests (LOT) in the tertiary units, as LOT data is not available for the Malm itself. S_h was thus determined to 19.6 kPa m^{-1}. In the absence of data on the friction angle and S_H, we assumed a critically stressed crust, following the calculation method of Zoback (2007), which calculates S_H as a function of pressure (P), S_h and the friction coefficient (μ) of the fault:

$$\frac{(S_H - P)}{(S_h - P)} = \left((\mu^2 + 1)^{\frac{1}{2}} + \mu\right)^2 \quad (19)$$

In this study, μ is assumed to be 0.6, which is a typical value for the faults in the underground that lack any measurement (Zoback 2007). A 34.6 kPa m^{-1} rate has been calculated for the S_H gradient in our study. The displacement BC is applied by fixing one face of the model while applying the corresponding stress on the opposite face. For example, in the y direction, the back side of the model is fixed at zero displacement, while a stress value is applied on the front side. The stress values in each principal direction are defined using a depth-dependent linear function. The stress magnitude is calculated based on the rock density and a direction-specific coefficient that represents the stress regime. In this study, the coefficient is set to 1.54 for the y-direction (corresponding to the ratio between S_H and S_h), while values of 1.0 and 0.77 are assigned to the z- and x-directions, respectively. A "homogeneous case" with a simplified homogeneous reservoir is developed to investigate the general THM response of the hydrothermal doublet and HT-ATES triplet.

The parameterization of the homogeneous case follows the studies of Egert et al. (2022), Bohnsack et al. (2021), and Potten (2020) and is presented in Table 1.

In addition to comparing the THM response of the two applications, the influence of heterogeneous permeability distributions on heat recovery and fault stability is investigated for the HT-ATES triplet. Table 2 presents the permeability differences across two heterogenous cases. The heterogeneity scheme and permeability values of each layer are synthetic and were constructed as representative end-member scenarios, informed by the general range and spatial pattern of karst-related permeability heterogeneity reported by Hörbrand et al. (2025), rather than derived directly from a specific field dataset. The wide permeability range adopted between the moderately and extremely heterogeneous cases (spanning more than three orders of magnitude) was chosen to bracket a plausible range of karst-related heterogeneity, from moderate to severe, rather than to represent a single most-likely field configuration. In the homogenous case the permeability of the six reservoir layers is identical and already mentioned in Table 1. The total flow rate in the topmost (30 m thick) reservoir layer of the homogenous case is 8.5 l s^{-1} while each of the lower five (100 m thick) layers has a flow rate of 28.3 l s^{-1}, resulting in a total flow rate of 150 l s^{-1}. The injection and production flow rates are also adapted according to the heterogeneity pattern of the reservoir layers. In the homogeneous case, each of the six layers has a flow rate determined solely by thickness, assuming constant permeability throughout the 530 m of the Malm reservoir. In contrast, the heterogeneous cases result in higher flow rates in the sections of the wells located in more permeable layers. While all three cases maintain the same total flow rate of 150 l s^{-1}, the distribution varies significantly. In the extremely heterogeneous case, the top layer accounts for only 5% of the reservoir's total volume but receives 45% of the injected/produced fluid. Hydraulically, this is comparable to the permeable karstic zones described by Hörbrand et al. (2025), although we have simplified its geometry into a single horizontal layer. These heterogeneity schemes

Table 1 Model parametrization scheme including material properties, operational conditions, geometric information, and simulation settings of the homogeneous case. Rock parameters are compiled from Egert et al. (2022), Bohnsack et al. (2021), and Potten (2020)

Parameters and units		Values
Simulation time [year]		10
Friction coefficient (μ) [-]		0.6
Orthogonal distance to the fault [m]	Well H/Well P	112
	Well C/Well I	178
Injection temperature [°C]	Well H	140 (summer)
	Well C/Well I	50 (winter)
Flow rate [l s^{-1}]	Injection	150
	Production	150
Permeability [m^2]	Reservoir	1.48×10^{-12}
	Cap rock and basement	9.8×10^{-17}
Porosity [-]	Reservoir	0.023
	Cap rock and basement	0.01
Specific heat capacity [JKg^{-1} K^{-1}]	Cap rock	2800
	Reservoir	2700
	Basement	2500
Thermal conductivity [Wm^{-1}K^{-1}]	Cap rock	2.1
	Reservoir	2.5
	Basement	3.2
Young modulus [GPa]	Cap rock	25
	Reservoir	53
	Basement	63
Poisson ratio [-]	Cap rock	0.36
	Reservoir and basement	0.29

Table 2 Reservoir layers with their thickness, permeability, and flow rate (Q) for different cases named as: the extremely and moderately heterogeneous cases

Layer	Thickness [m]	Case			
		Extremely Heterogeneous		Moderately Heterogeneous	
		Permeability [m^2]	Q [l s^{-1}]	Permeability [m^2]	Q [l s^{-1}]
Res 1	30	1.18×10^{-11}	67.9	4.9×10^{-12}	28.3
Res 2	100	2.81×10^{-12}	53.7	3.4×10^{-12}	65
Res 3	100	1.48×10^{-12}	28.3	1.48×10^{-12}	28.3
Res 4	100	9.8×10^{-15}	0.02	1.48×10^{-12}	28.3
Res 5	100	9.8×10^{-15}	0.02	9.8×10^{-15}	0.02
Res 6	100	9.8×10^{-15}	0.02	9.8×10^{-15}	0.02

offer insight into the more realistic processes governing the THM response of the Malm reservoir compared to the homogeneous parametrization.

Results

Thermo-hydraulic response of the reservoir

Figure 3a shows the thermal plumes, both hot and cold, with depth-dependent radii around Well H and Well C after 10 years of operation for the homogeneous case of the HT-ATES triplet. Due to the temperature-dependent density effect, the injected hot fluid accumulates on top, while the denser cold fluid descends within the reservoir. The radius of the cold plume around Well C is larger than the hot plume around Well H, because Well C is not used for production, allowing the injected fluid to propagate further into the reservoir. Well I in the hydrothermal doublet operates throughout the year, unlike the 6-month periods of the HT-ATES triplet, resulting in a more extensive cold front around Well I (Fig. 3b). Meanwhile, Well B in the HT-ATES triplet and Well P in the hydrothermal doublet remain unaffected by temperature changes, as they only extract the ambient reservoir fluid. Under the specific well spacing, permeability distribution, operational conditions, 10-year simulation duration, and several other modelling assumptions considered here, the hydrothermal doublet simulation does not show thermal breakthrough.

Figure 3c shows the temperature signal along the line introduced in Fig. 3a, labeled as top and bottom depending on depth. The top curves correspond to a depth of 1485 m, located at the top of the reservoir, while the bottom curve in Fig. 3c correspond to the data from a depth of 1980 m, located at the bottom of the reservoir. Comparing the two depths shows that the cold front extends significantly farther at the bottom of the reservoir, while the hot plume does at the top. For example, after the last hot water production phase, the temperature at Well H reaches 132 °C at the top of the reservoir, compared to only 118 °C at the bottom. This asymmetry reflects the density contrast between hot and cold water as the buoyant hot water accumulates preferentially near the top of the reservoir, while the denser cold water sinks and spreads along the base.

Due to the high transmissibility of the reservoir, the pressure changes resulting from production and injection operations are minimal. The pressure perturbation near Well I is slightly greater than that near Well P, primarily due to temperature effects. After 10 years, the simulated pressure difference ranges from −0.1 to + 0.1 MPa (Fig. 3d). The pressure difference is measured as the difference between the IC pressure and operation-induced pressure perturbations. For example, at the exact location of the wells, the pressure after 10 years of operation is 0.1 MPa either higher (in case of injecting fluid) or lower (in case of producing fluid) that the pressure value of the same spot at the IC. The pressure changes are nearly identical for the HT-ATES and hydrothermal doublet, therefore only the 3-D view of the hydrothermal doublet is presented.

Mechanical response of the reservoir

The mechanical response of the two applications differs, primarily due to the propagation of the cold front. Changes in effective stress along the direction of maximum horizontal stress (north) are depicted in Fig. 3e and f. Similar to the temperature distribution, the affected volume around Well C in the HT-ATES triplet is larger than that around Well H. The injection of cold fluid causes contraction of the porous matrix (thermoelasticity) and increases pressure (poroelasticity), leading to a reduction in effective stress around Well C. In contrast, around Well H, the matrix expands due to thermoelasticity, resulting in an increase in effective stress. A maximum increase of 13 MPa in effective stress in the y/north direction is observed near Well H after the last winter period. For the hydrothermal doublet, the affected volume around Well I is larger than that around Well C of the HT-ATES triplet. The absolute change in effective stress magnitude increases from 17 MPa near Well C of the HT-ATES triple to 18 MPa near the Well I of the hydrothermal doublet. During the 6-month resting period at Well C, the advancement of the cold front is stopped and the rate of temperature change diminishes. As a result, the thermally induced contraction slows down or ceases, and the stress state begins to partially recover toward its initial condition. This transient response is attributed to the redistribution of the effective stress, particularly near the top of the reservoir, where reduced cooling can locally result in expansion (limited reddish area next to Well C in Fig. 3e). The negligible pressure difference (see Fig. 3d) indicates that poroelastic effects have an insignificant impact on the geomechanical response of the reservoir, with thermoelasticity being the dominant factor. Although pressure perturbations propagate rapidly and over large distances within the reservoir, their magnitude remains small in this case, resulting in only minor poroelastic stress contributions. This is further supported by the absence of noticeable mechanical changes around Well B, where pressure effects are present but insufficient to induce a significant geomechanical response. The very high permeability of the Malm reservoir (1.48×10^{-12} m^2) is the main reason behind the negligible poroelasticity.

Displacement values are calculated for both applications as a result of the effective stress changes. Similarly to stress, displacement is calculated in three directions. Figure 4 shows the magnitude of displacement in the z-direction for

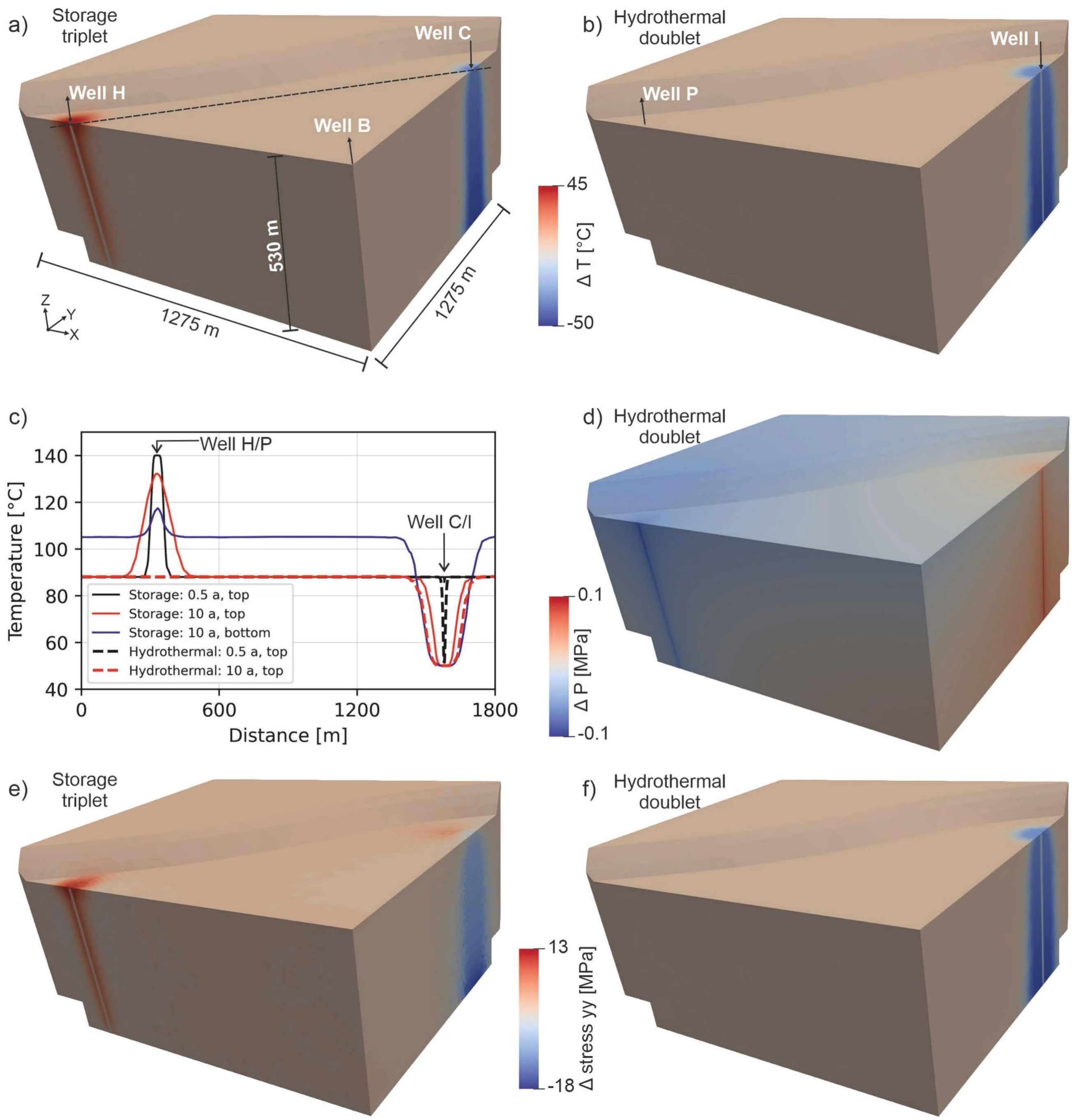

Fig. 3 Temperature changes (ΔT) after 10 years of operation for the HT-ATES triplet (**a**) and the hydrothermal doublet (**b**). The time for the triplet corresponds to the last hot fluid production, i.e. the last winter period. The locations of the hot, cold, and buffer wells are highlighted via arrows and their names (Well H, Well C, and Well B) in subplot a. Dimension and orientation of the next 3-D visualizations remain the same as presented in subplot a. **c**) The dashed cross-section line in subplot a is used to plot the temperature values versus the distance between Well H and C of the HT-ATES and also Well I and P of the hydrothermal doublet. The solid black and red curves represent the temperature across the top of the reservoir (1485 m) after 0.5 and 10 years of the HT-ATES operation, respectively. The solid blue curve represents the temperature across the bottom of the reservoir (1980 m) after 10 years of the HT-ATES operation. The dash black and red curves represent the temperature across the top of the reservoir (1485 m) after 0.5 and 10 years of the hydrothermal doublet operation, respectively. The locations and names (Well P and Well I) of the production and injection well are also highlighted in subplot b. **d**) Pressure changes (Δ P) after 10 years of operation in the hydrothermal doublet. Changes of effective stress in the y direction (Δ stress yy) or north after 10 years of the operation for the HT-ATES triplet (**e**) and the hydrothermal doublet (**f**)

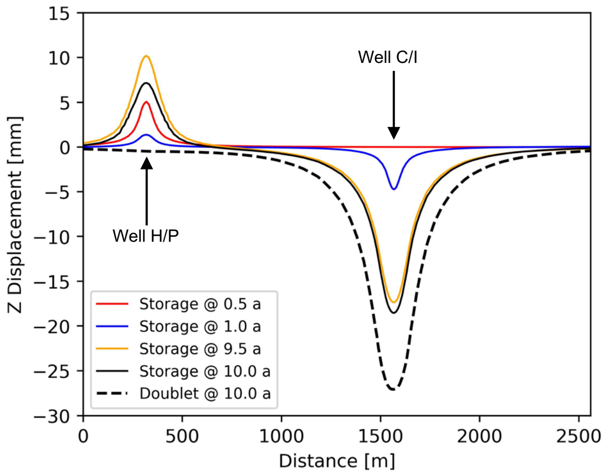

Fig. 4 Displacement variation for different cycles of the HT-ATES triplet and the hydrothermal doublet along the dashed cross-section line in subplot Fig. 2a. For the hydrothermal doublet, only one time slot is plotted due to the monotonic behaviour of the system, i.e. continuous increase of the subsidence at the Well P location throughout time. Locations of the Well H (for the HT-ATES)/P (for the hydrothermal doublet) and Well C (for the HT-ATES)/I (for the hydrothermal doublet) are marked by black arrows

the HT-ATES triplet and the hydrothermal doublet, with data extracted from the top of the reservoir. The trace of the plotted data is along the cross section line shown in Fig. 3a. Due to the alternating operational mode of the HT-ATES, displacement varies across the operational phases of Well C and H. At Well H, displacement decreases from month 6 (0.5 years) to month 12 (1 year) as the well withdraws the injected heat during this 6-month winter period. In this scenario, Well C exerts a greater influence on displacement magnitude compared to Well H, as the cold water is not withdrawn from the reservoir. After 10 years of operation, the displacement at the top of Well H (HT-ATES) is 8 mm. At the same time, the computed displacement at Well C is 19 mm. The expansion caused by positive temperature changes near Well H leads to uplift, while the matrix contracts at Well C due to the injection of cold fluid that leads to subsidence. Between years 9.5 and 10, the displacement at Well C changes only slightly compared to the corresponding change at Well H. This asymmetry arises from the different operational modes of the two wells. Well C operates unidirectionally and by year 9.5 it has already undergone nine prior injection cycles, and the surrounding stress field has approached a quasi-steady state, such that the additional perturbation induced during the tenth cycle is comparatively small. Well H, in contrast, is bidirectional: between years 9.5 and 10 it operates in production mode (winter period), which reduces its geomechanical impact during this interval relative to the previous 6-month period between years 9.0 and 9.5.

In comparison, the classic hydrothermal doublet exhibits a greater absolute impact on displacement than the HT-ATES scenario at the location of the Well I (28 mm) versus the location of the Well C (19 mm). At Well P, the doublet shows negligible displacement, shown as a dashed line in Fig. 4, since Well P only produces reservoir fluid at ambient temperature and therefore has no thermoelastic impact. The observed volumetric expansion is attributed to the temperature change itself rather than to the injected fluid mass, since the associated pressure changes remain small.

Within the adopted linear elastic constitutive framework, the model cannot capture cumulative or path-dependent effects such as fatigue, damage accumulation, or thermo-mechanical degradation across cycles. Therefore, the elastic response depends only on the instantaneous stress and temperature state, not on loading history. The lower displacement at the HT-ATES triplet therefore does not reflect any cyclic conditioning or degradation-limiting mechanism. Instead, it reflects the reduced cumulative thermal perturbation associated with intermittent operation. Notably, Well I of the hydrothermal doublet injects twice the volume of cold water injected by Well C of the triplet. The higher displacement around Well I is therefore driven by this larger injected volume, not solely by the choice of geothermal concept.

To assess the potential of fault stability, a slip tendency analysis was conducted. This analysis is based on highly conservative assumptions, namely that the Malm aquifer is critically stressed and shares the same elastic properties as the overburden units. The wells, particularly Well C, are intentionally positioned in close proximity (178 m) to the most critical section of the fault. This placement aims to enhance understanding of the THM processes, as fault destabilization would otherwise be negligible. However, in realized geothermal projects within the Malm reservoir, injection well trajectories are typically designed to avoid critical fault regions to minimize risks.

The first notable point is that the fault surface, with its complex geometry (spatially varying strike and dip), exhibits a wide range of normalized initial slip tendency values between 0 to 0.76 (Fig. 5a). The highest values are found in areas where the fault surface is oriented with a 30° angle to the maximum horizontal stress (y direction), i.e., the northward orientation.

A closer examination of the normalized slip tendency changes after 10 years of operation in both the HT-ATES triplet and hydrothermal doublet is presented in Fig. 5b and c, respectively. In the HT-ATES system, the fault surface is primarily influenced by Well C, with a lesser impact from Well H. In the hydrothermal doublet, Well P does not perturb the normalized slip tendency due to the lack of any temperature changes and the negligible influence of poroelasticity. The maximum increase in the normalized slip tendency is calculated to be 0.137 adjacent to the Well I. The increased normalized slip tendency for the hydrothermal doublet is mainly concentrated in the deeper sections of the fault

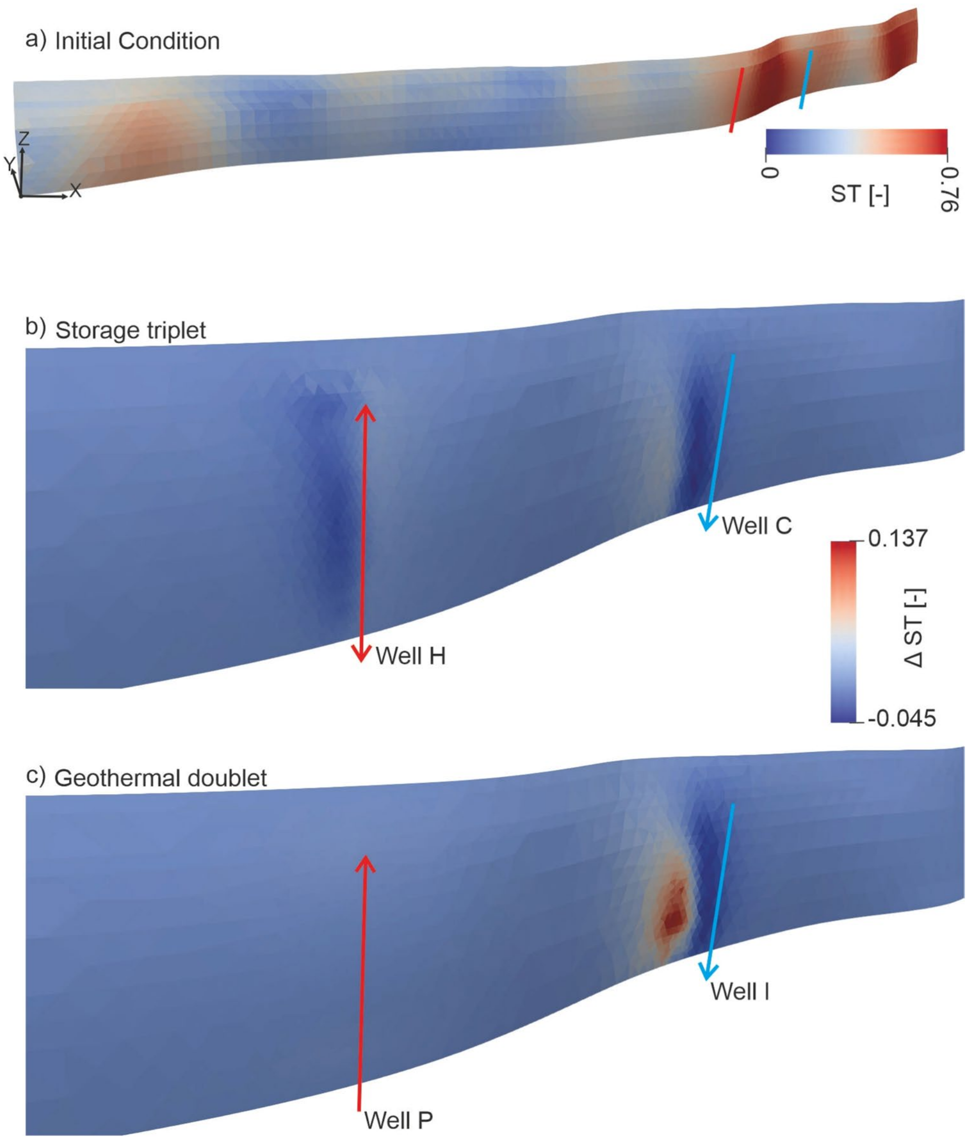

Fig. 5 **a**) Normalized slip tendency (ST) distribution on the fault surface at the initial condition. Normalized ST changes (Δ ST) in a zoomed part of the fault at the end of the simulation, i.e.10 years of operation, for the HT-ATES triplet (**b**) and hydrothermal doublet (**c**). The scale of the subplot a is different from b and c, due to the different range of values. Wells are visualized and labeled accordingly

surface due to the accumulation of the cold plume in deeper parts and also the shorter distances between the fault surface and Well I. The red patch in Fig. 5c highlights this maximum increase of the normalized slip tendency. For the HT-ATES triplet, the increase in the normalized slip tendency is lower, with a maximum change of + 0.03. The higher risk of the hydrothermal doublet is due to the continuous injection of the cold water rather than a cyclic operation. For both applications, the changes after 10 years do not lead to fault destabilization as the normalized slip tendency remains significantly below the threshold (1.0).

The normalized slip tendency perturbation exhibits a mirrored pattern adjacent to each well: a primary zone of destabilization (or stabilization) directly around the well is bordered by a narrow zone of opposite sign. The alternating positive and negative changes in normalized slip tendency surrounding the wells are a consequence of the localized thermoelastic stress redistribution. Heating induces thermal expansion of the surrounding rock, increasing compressive normal stresses in the immediate vicinity of the Well H while reducing them in adjacent regions to satisfy elastic equilibrium. Conversely, cooling causes thermal contraction, reducing normal compression near Well C/I and producing compensating increases in compression farther away. Because the normalized slip tendency is defined as the ratio between shear stress and effective normal stress, these opposing perturbations in the normal stress generate the observed mirrored pattern of increased and decreased slip tendency on either side of the thermally affected zone.

The impact of heterogeneity

Figure 6 shows the differences in the thermal recovery efficiency (ϵ) across the three reservoir parametrizations used for the HT-ATES simulations. The thermal recovery

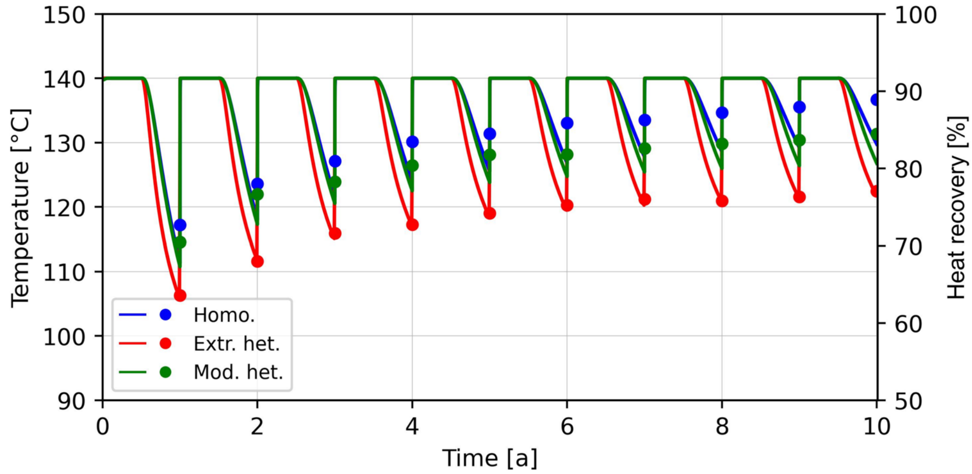

Fig. 6 Temperature and heat recovery efficiency evolution over 10 years of hot fluid injection and production at Well H location. Temperature data are extracted from top of the Well H. The temperature curves for the homogeneous (Homo.) case and the extremely (Extr. het.) and moderately (Mod. het.) heterogeneous cases are plotted by blue, red, and green curves, respectively. The heat recovery efficiency scatter plots for the homogeneous case and the extremely and moderately heterogeneous cases are plotted by blue, red, and green circles, respectively

efficiency is an important parameter for the thermal performance of heat storage systems and is defined as the ratio between total extracted and stored energy:

$$\epsilon = \frac{\int (T_{out}(t) - T_{res})\, dt}{\int (T_{in}(t) - T_{res})\, dt} \quad (20)$$

where, $T_{out}(t)$ is the produced temperature form Well H over time, T_{res} is the reservoir temperature (85 °C in our case), $T_{in}(t)$ is the injected temperature over summer period in Well H (140 °C). While the nominator of the equation is a true integral, the denominator is a fixed value as T_{res} and $T_{in}(t)$ are constant.

The conventional hydrothermal doublet was not included in this analysis. The temperature data refer to the top of the Well H. While heat recovery improves throughout the storage operation, it varies among the three cases. In the homogeneous case, with the highest recovery improving to c. 90% after 10 years, the hot fluid is injected and produced across the entire thickness of the permeable reservoir (totaling 530 m). Such a high reservoir thickness allows for better heat accumulation and storage over time. In contrast, the two heterogeneous cases significantly limit the available storage space. The heat recovery in the heterogeneous cases shows noticeable heat losses compared to the homogenous case with a c. 10% lower efficiency. The high transmissibility of the reservoir causes heat to be transported away from the wells via advection. In the extremely heterogeneous case, heat loss in the uppermost reservoir unit leads to a reduced heat recovery.

Figure 7 illustrates the impact of heterogeneity on the normalized slip tendency of the fault surface after 10 years of operation. Compared to the homogeneous case, both heterogeneous cases show a slightly greater impact on normalized slip tendency. While the maximum increase in normalized slip tendency is calculated to be 0.03 for the homogeneous case, it increases to 0.04 for both the moderately and extremely heterogeneous cases. This higher impact in the heterogeneous cases is attributed to a higher amount of the total flow occurring in the uppermost part of the reservoir. While Fig. 7a shows the uniform change of the normalized slip tendency along the homogeneous reservoir, two different heterogeneity patterns resulted in different distribution of the normalized slip tendency. The figure also shows an irregular distribution of the normalized slip tendency changes, which is caused by both the distance between the fault and the wells, as well as the petrophysical properties of the six reservoir layers. In the homogeneous case, with uniform permeability and flow rate distribution, the changes in normalized slip tendency closely correspond to the distance between the wells and the fault surface (see Fig. 5b and Fig. 7a). In the extremely heterogeneous case, the uppermost layer has the highest permeability and flow rate, but it is also farther from the fault surface compared to the other layers, as the fault is slanted (see Fig. 2b). Despite this higher distance, the increase in normalized slip tendency in the uppermost layer (Fig. 7a) suggests that the stress changes due to the strong cooling of this layer overcompensates the larger distance.

In the moderately heterogeneous case, the in normalized slip tendency changes are concentrated in the middle part of the reservoir, although the uppermost layer has the highest permeability. The depth shift of the red patch, with a large normalized slip tendency increase, can be seen in Fig. 7b and c. This is caused by two effects: firstly, the fault is closer to the deeper part of the reservoir and the permeability contrast is only moderate. Secondly, due to density-driven convection, the cold plume migrates towards the bottom of the reservoir, which means that the uppermost zones receive less thermal perturbation. Therefore, shifting the highly transmissible zones to the deeper layers of the Malm reservoir can enhance the risk for specific sections of the fault surface.

Near Well H of both cases, the thermal expansion increases the normal stress, reducing the normalized slip tendency (blue patch in Fig. 7b and c). The depth of the blue

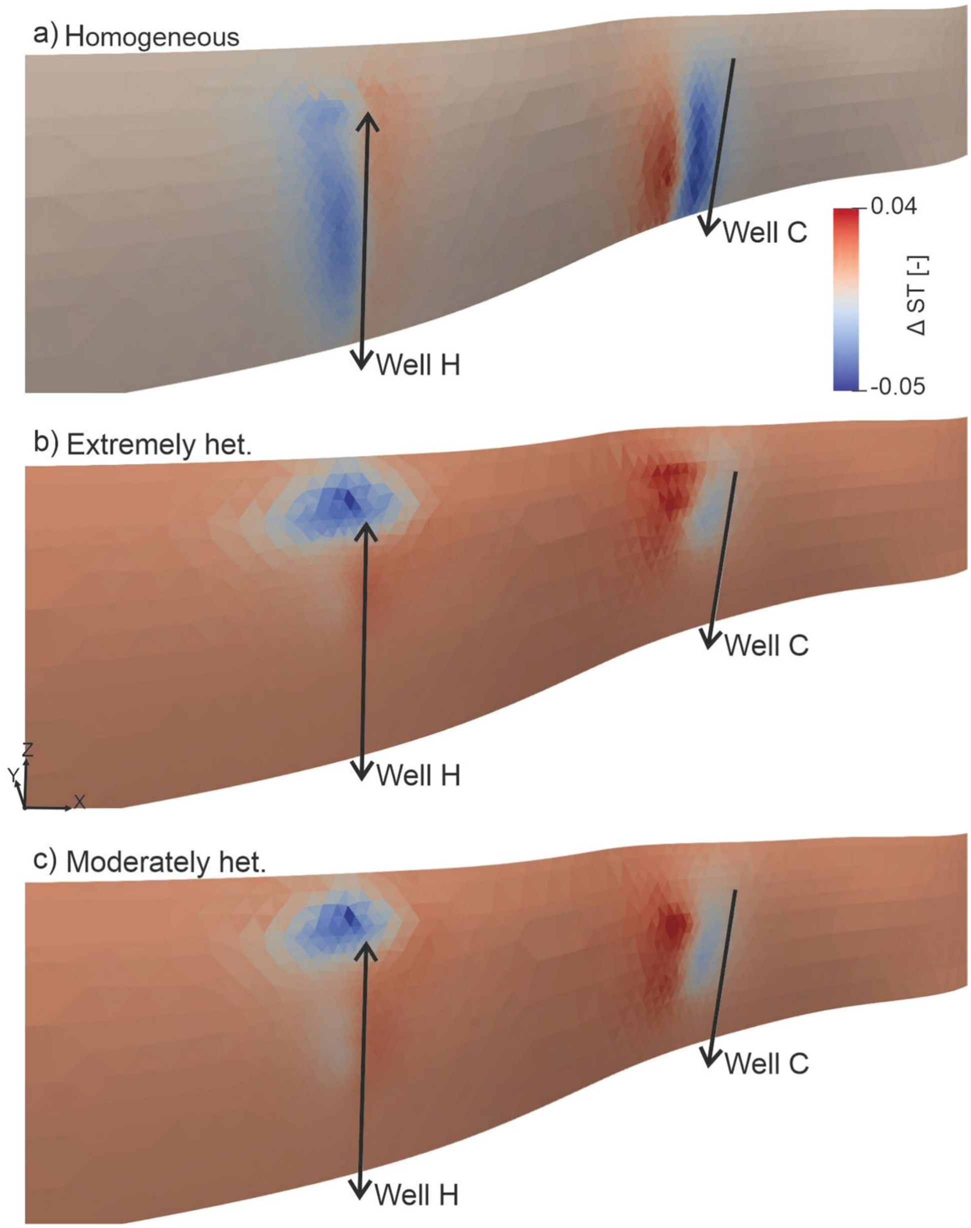

Fig. 7 Normalized slip tendency changes after 10 years of the storage operation in the homogenous (**a**), extremely (**b**) and moderately (**c**) heterogeneous cases. The scale remains the same in three subplots. Two wells, Well H represented by a bidirectional arrow and Well C represented by a unidirectional arrow, are labeled accordingly. The same data is used to plot subplot a and Fig. 5b

patch, indicating the decreased normalized slip tendency, does not change from extremely to moderately heterogeneous cases due to the accumulation of the hot plume at the top of the reservoir. Although the extremely heterogeneous case injects more heat into the uppermost 30-m layer of the reservoir, the heat accumulation or reduction in normalized slip tendency.

shows no significant difference to the moderately heterogeneous case.

Long-term thermo-hydro-mechanical response

Under the investigated assumptions, the normalized slip tendency remained below the threshold throughout the 10-year simulation period, even under conditions of strong heterogeneity and unrealistically short distances between the wells and the faults. However, the increasing normalized slip tendencies caused by the propagation of cold water around Well C over time could pose risks for the long-term operation of HT-ATES projects. An additional simulation with a 50-year duration was conducted to extend the process understanding towards a longer-term, scenario-based assessment of fault stability analysis for HT-ATES operations. For these long-term simulations, the extremely heterogeneous HT-ATES case was selected, as it combines the highest permeability and flow rate contrast among the investigated scenarios.

The cold front propagation over time around well C (of the HT-ATES triplet) is visualized in Fig. 8. Over time, the

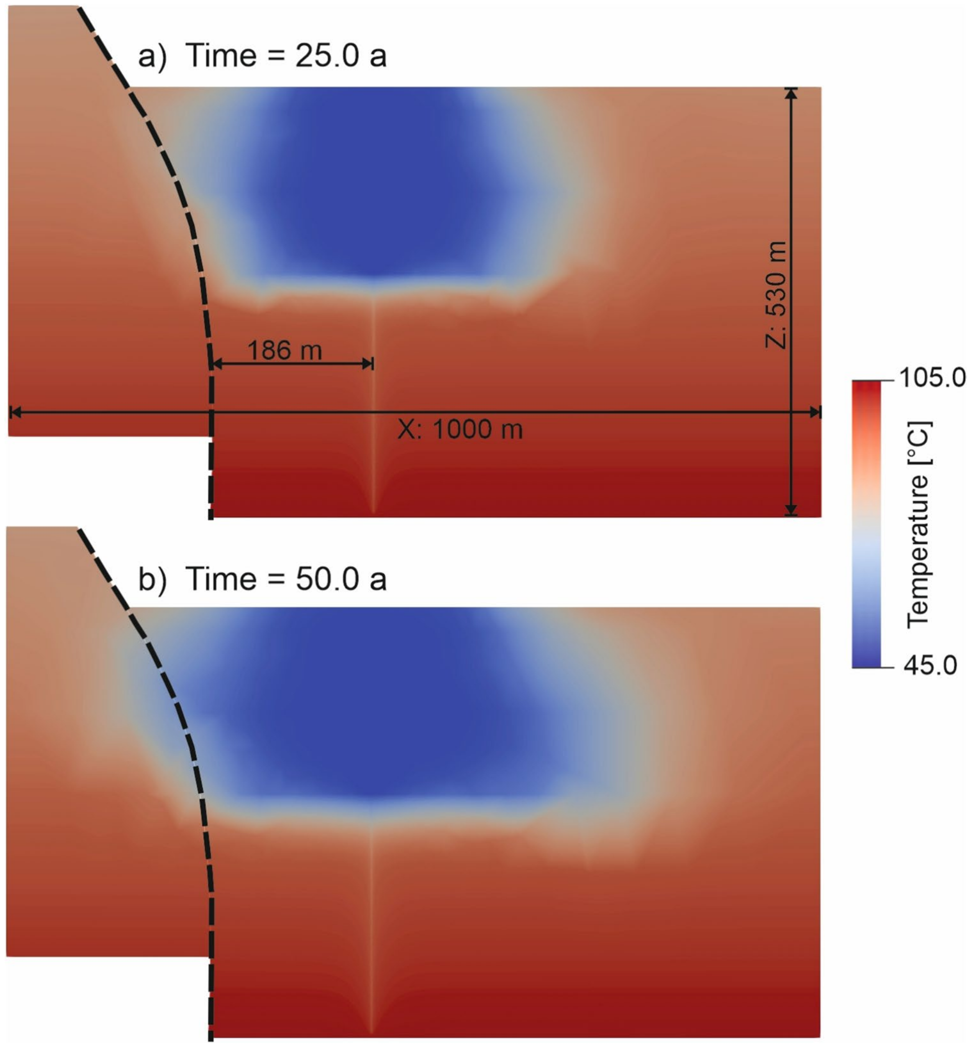

Fig. 8 Cold front propagation after 25 (**a**) and 50 (**b**) years of simulations. The fault trace is plotted as a black dashed line. The slice is perpendicular to the y direction, hence the distance between the fault trace and Well C is 186 m, which is slightly higher than the orthogonal distance. The extension of the 2D slice is 1000 m × 530 m

cold front extends into the permeable section of the Malm reservoir. In the extremely heterogeneous case, only 230 m of the 530 m thick Malm formation is effectively utilized as a reservoir. The injection rate in the lower part of the reservoir is very low, and only a slight temperature anomaly can be detected around the injection points. In this 50-year simulation, the typical inverse funnel-shaped cold plume, as shown in Fig. 3b, does not form due to the strongly increased permeabilities of the three uppermost reservoir layers. By the end of the 50 years, the cold front reaches the fault surface. However, on the fault surface the increase in the normalized slip tendency remains below the critical threshold (Fig. 9a). Although the temperature signals (both cold and hot) have already reached the fault surface (Fig. 8b) the thermoelastic impact is not substantial enough to reactivate the fault. After 50 years of operation, the maximum normalized slip tendency reaches 0.9 in the most critical sections of the fault surface. Compared to the 10-year simulations, the additional 40 cycles of cold water injection increased normalized slip tendency change from 0.04 to 0.2.

The alignment of the temperature and normalized slip tendency patterns on the fault surface (Fig. 9a and b) highlights the significant role of thermoelasticity in the Malm reservoir. The density-driven accumulation of both cold and hot plumes is also evident (see Fig. 9b) on the fault surface after 50 years of HT-ATES operation.

Discussion

This study compares the geomechanical response, specifically the fault stability analysis, of a hydrothermal doublet and an HT-ATES triplet operating in a faulted Malm reservoir. In both applications, thermoelasticity is identified as the dominant factor governing the dynamic geomechanical response of the reservoir, with poroelastic effects remaining minor due to the high permeability of the Malm aquifer and the correspondingly small pressure perturbations. For the operating scenarios considered here, the HT-ATES triplet induces smaller THM perturbations than the hydrothermal

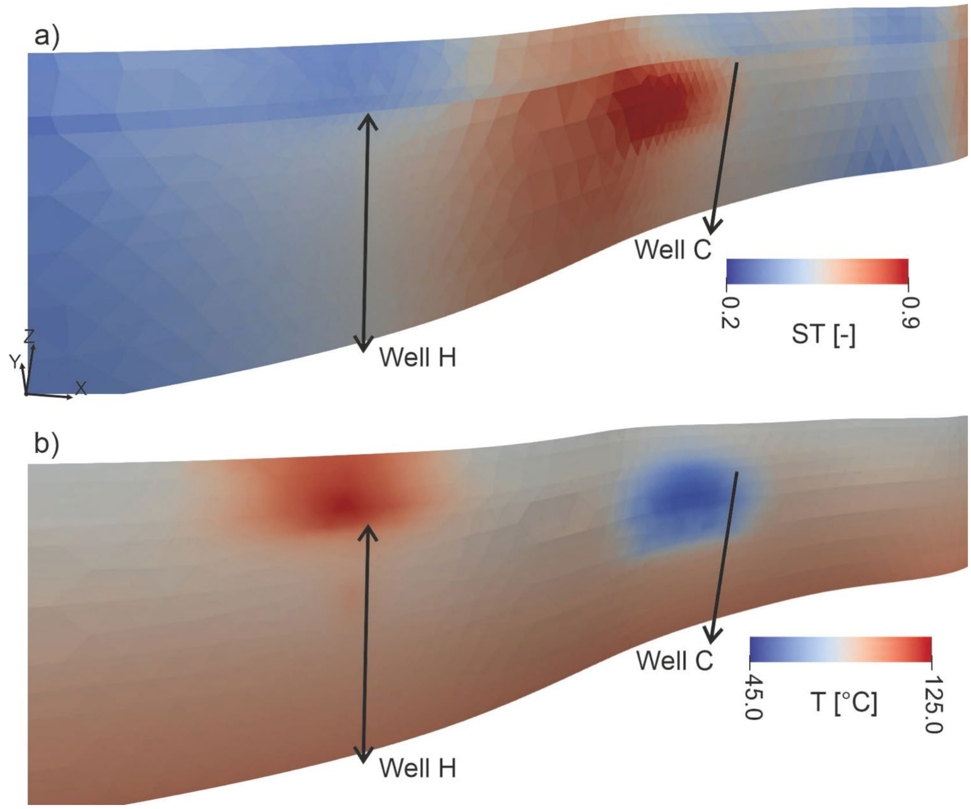

Fig. 9 Normalized slip tendency (**a**) and temperature (**b**) change on the fault surface after 50 years of HT-ATES operation. Well H and C are labeled and represented with bi and uni-directional arrows, respectively

doublet, due in part to its cyclic thermal loading and lower cumulative thermal disturbance. Since thermoelasticity is the primary factor in reservoir deformation and fault stability, a smaller temperature difference between the ambient matrix and the injection fluid limits the associated thermal stress perturbations and slip-tendency changes.

The magnitude of the predicted displacement is consistent with the order of magnitude reported in previous studies (Birdsell and Saar 2020; Stricker et al. 2024). Most published investigations focus on surface deformation measured using satellite-based geodetic techniques, whereas the displacements reported here correspond to the reservoir depth. Stricker et al. (2024) demonstrated that thermoelastic deformation attenuates rapidly away from the thermally affected zone because heat propagation is spatially limited. Consequently, the displacements computed in the present study are expected to have potentially a limited expression at the ground surface, particularly given the negligible poroelastic contribution associated with the high permeability of the Malm reservoir. The maximum predicted vertical displacement of 28 mm at a depth of 1470 m does not, by itself, necessarily imply mechanical integrity issues; however, a dedicated well integrity assessment would be required to quantify its implications for the well system. Such displacement magnitudes are well within the resolution of conventional downhole monitoring techniques, including borehole strainmeters (DeWolf et al. 2015) and borehole extensometers (Gholinia et al. 2022).

The thermal expansion of the heated matrix (e.g., near Well H of the HT-ATES triplet) predominantly increases normal stress, thereby reducing the normalized slip tendency and stabilizing the reservoir. In contrast, cooling in the vicinity of Well C (of the HT-ATES triplet) or Well I (of the hydrothermal doublet) has a destabilizing effect. The onset of fault destabilization in the vicinity of the cold/injection wells can be observed as reduced injection pressure or increased injectivity in real operation (Zhou et al. 2009; Koh et al. 2011; Gan and Elsworth 2014).

The investigation of heterogeneity scenarios reveals that thin zones of elevated permeability, such as those caused by karstification, pose a risk to the mechanical stability of faults. In these cases, stress changes reach the fault more quickly and with greater intensity. While such zones are typically advantageous as they have the capacity for high injection flow rates without any significant pressure increase, our simulations showed they can induce significant localized stress changes in small areas of the fault. However, the magnitude of potentially induced seismicity is expected to remain limited due to the restricted extent of critical areas (Shapiro et al. 2007).

Beyond the simulation results presented here, these findings carry broader engineering implications for the planning and monitoring of deep geothermal projects, particularly near populated areas such as Munich. Matrix failure often produces acoustic emissions, which can be detected by a seismic monitoring network (Stanchits et al. 2015) like distributed acoustic sensing (DAS) (Lindsey et al. 2020). Decades of experience with intense injection/production operations in the hydrocarbon industry provide valuable insights into deploying such networks effectively (van der Baan et al. 2013). All major seismic events in the Munich area have been recorded in proximity to (cold) injection wells (Megies and Wassermann 2014; Seithel et al. 2019), suggesting the vicinity of cold wells as a plausible location for such monitoring, although the present study does not itself model or evaluate monitoring network design. Computed effective stress changes and induced displacement in this study underscore the broader need for geomechanical risk assessment during the planning of any deep geothermal project.

Limitations

The comparison presented in this study should be interpreted in the context of the investigated operational scenarios. The HT-ATES triplet and hydrothermal doublet serve different engineering purposes and are characterized by fundamentally different thermal loading histories. While the hydrothermal doublet continuously extracts heat from the reservoir, the HT-ATES system operates cyclically with alternating injection and production phases. Consequently, the lower THM perturbations observed in the HT-ATES case may partly reflect the reduced cumulative thermal loading associated with cyclic operation rather than an intrinsic advantage of HT-ATES technology. A rigorous comparison of the two concepts would require normalization with respect to delivered thermal energy, storage capacity, or equivalent economic and operational objectives.

Given the high computational demands of numerical simulations for coupled THM processes, the simulation period was constrained to 10 injection and production cycles (i.e., 10 years) for the homogeneous and moderately heterogeneous cases. As a result, operational decision-making will not be derived from these short-term simulations. However, to facilitate the transfer of improved process understanding to the long-term safe operation of HT-ATES, an additional simulation was conducted over a 50-year period for the extremely heterogeneous case. All of the scenarios are based on conservative assumptions to assess the necessary distance from fault systems to ensure geomechanical stability throughout the operational lifespan of HT-ATES.

The present work focuses on the THM response of HT-ATES systems under a prescribed thermal loading scenario. The continuous availability of a heat source capable of providing injection temperatures of 140 °C is not evaluated, as techno-economic assessment of heat supply lies beyond the scope of this study. The selected injection temperature represents a plausible operating condition for HT-ATES systems coupled to industrial waste heat streams, geothermal resources, concentrated solar thermal plants, or surplus renewable energy converted to heat (Heldt et al. 2024; Dobson et al. 2025).

The present study adopts an equivalent porous-medium representation of the Malm reservoir. Although this approach captures the large-scale THM response relevant to the comparative assessment, it cannot explicitly resolve preferential flow through karst conduits or discrete fractures. Instead, the influence of karstification is approximated through heterogeneous permeability distributions containing localized high-permeability zones. While this representation reproduces the first-order effects of hydraulic heterogeneity, explicit modelling of karst conduits or discrete fracture networks could lead to different local flow paths, thermal breakthrough behaviour, and stress perturbations. Furthermore, only two deterministic heterogeneous configurations were investigated. Reservoir heterogeneity is one of the principal factors identified in this study. However, it remains unclear how strongly the reported thermal recovery and fault stability results depend on the specific permeability distributions considered here. Alternative heterogeneity patterns such as stochastic permeability fields, discrete fracture networks, or fault-controlled preferential flow paths could lead to different outcomes. Such models would provide a valuable extension of the present work.

The adopted numerical framework is based on a saturated, single-phase thermo-poroelastic formulation with a linear elastic mechanical constitutive law. Consequently, the model does not capture irreversible or nonlinear processes that may become relevant under repeated thermal cycling, including plastic deformation, thermal softening, fatigue, damage accumulation, fracture propagation, or constitutive memory effects. This limitation should be considered when interpreting the cumulative effect of repeated thermal cycles over the simulated 10- and 50-year periods, as such processes could progressively alter the mechanical response in ways not represented by a purely elastic formulation. Permeability is also held constant throughout the simulations. Thermo-mechanically induced changes in permeability for instance through matrix deformation or damage near the wells or fault are not represented. Such changes could influence both the hydraulic and geomechanical response computed here.

Because thermoelasticity was identified as the dominant factor governing the geomechanical response, the robustness of the reported stress perturbations, displacements, and slip-tendency changes depends strongly on the modelling assumptions (Sect. "Model Description"). This dependence is particularly relevant given that the reported stress perturbations are substantially larger than the pressure perturbations, which underlies the conclusion that thermoelastic effects dominate over poroelastic effects. No dedicated parametric sensitivity analysis on these material properties was performed in the present study, hence the results should therefore be interpreted as conditional on the adopted thermoelastic parameter set. A systematic sensitivity analysis of these parameters (Table 1) would be a valuable extension of this work.

Herein, the numerical model represents a synthetic geological configuration inspired by the faulted Malm reservoir in northern Munich, rather than a site-specific model calibrated to a particular setting. While this approach is appropriate for the comparative assessment presented here, the transferability of the specific quantitative results (e.g., slip-tendency magnitudes, displacement values) to a specific site should be made with caution. Site-specific applications would require calibration against local geological, hydraulic, and geomechanical data.

Conclusions and outlook

In the scope of the presented study, the geomechanical responses of a classic hydrothermal doublet and an HT-ATES triplet have been compared using coupled numerical simulations, based on a synthetic geological model and a set of specific modelling assumptions. Under these conditions, thermoelasticity was identified as the dominant factor influencing the dynamic geomechanical response of the reservoir in both applications.

For the specific scenarios considered in this study, HT-ATES generated smaller THM perturbations, due in part to its cyclic thermal loading and lower cumulative thermal disturbance. Compared to the typical conditions of a conventional hydrothermal doublet, the operation of a HT-ATES system leads to lower displacements and risk of fault destabilization as investigated herein. After 10 years, the displacement at the Well H is 8 mm, lower than the displacement observed at Well C (19 mm) or Well I of the hydrothermal doublet (28 mm).

The highly complex orientation of the fault surface in the model results in a wide range of normalized slip tendency values, varying from 0 to 0.76 under the initial conditions. The hydrothermal doublet leads to perturbations in the normalized slip tendency, which are 4x higher (0.13 versus 0.03), compared to the HT-ATES triplet.

The examination of heterogeneous scenarios with thin zones of elevated permeability has shown a complex interplay between cooling front propagation and fault distance, which stresses the need for THM simulations. In general, high permeability zones, to be assumed as karstified units, increase the risk of the cold front reaching the fault faster than in homogeneous simulations.

Under our modelling assumptions and simplifications, the long-term (50-year) simulation also did not result in fault destabilization in the extremely heterogeneous case. However, the increase in the maximum normalized slip tendency changes from 0.04 to 0.2, highlighting the impact of additional cold water injection cycles.

This study also accentuated the importance of fault geometry by evaluating the influence of the distance between the fault surface and the wells. It demonstrated that small zones of the fault exhibit elevated normalized slip tendencies due to their orientation to the stress field. However, fault interpretation and interpolation are inherently subject to uncertainty. Unlike the deterministic model used in this study, a broader range of geological models, developed based.

on different interpolation algorithms, could be employed to account for a wider variety of potential geometries.

Future work should perform energy-normalized comparisons to provide a more rigorous assessment of the relative THM impacts of HT-ATES and hydrothermal doublets. To fully assess the potential risks, the simulations should account for the possibility of fracturing (exact time, location, and extent) and plastic deformation of the matrix. Modelling the wells as three-dimensional volumes, rather than as 0-D points, and coupling them into the reservoir model would enable a more accurate assessment of well stability.

Acknowledgements Ali Dashti received financial support from The German Academic Exchange Service (Deutscher Akademischer Austauschdienst: DAAD) to do his PhD in Germany as the Research Grants-Doctoral programmes in Germany 2019/20. This organization is appreciated for giving the opportunity to researchers. This study is part of the subtopic "Geoenergy" in the program "MTET—Materials and Technologies for the Energy Transition" of the Helmholtz Association. The work on this project from Thorsten Hörbrand and Kai Stricker was conducted
within the VESTA project funded by the German Federal Ministry for Economic Affairs and Energy (grant number 03EE4033D). Fruitful comments of Robert Egert regarding the numerical modelling are wholeheartedly acknowledged. Authors sincerely thank the three anonymous reviewers for their careful evaluation of the manuscript and for their constructive and insightful comments, which have helped us improve the quality and clarity of the work.

Author contribution AD did the conceptualization, coding, software, evaluation, and writing KS did conceptualization, and writing TH did conceptualization, and writing RB did coding, and software KB prepared geological model TK did conceptualization, and writing.

Funding Open Access funding enabled and organized by Projekt DEAL.

Data availability No datasets were generated or analysed during the current study.

Declarations

Competing interests The authors declare that they have no conflict of interest.

References

Aliyu MD, Chen H-P (2017) Sensitivity analysis of deep geothermal reservoir: effect of reservoir parameters on production temperature. Energy 129:101–113. https://doi.org/10.1016/j.energy.2017.04.091

Barbier E (2002) Geothermal energy technology and current status: an overview. Renew Sustain Energy Rev 6:3–65. https://doi.org/10.1016/S1364-0321(02)00002-3

Bloemendal M, Olsthoorn T, Boons F (2014) How to achieve optimal and sustainable use of the subsurface for aquifer thermal energy storage. Energy Policy 66:104–114. https://doi.org/10.1016/j.enpol.2013.11.034

Bloemendal M, Van Esch MS, Vardon PJ et al (2022) Novel ATES triplet system for autarkic space heating and cooling. IOP Conf Ser Earth Environ Sci 1085:012028. https://doi.org/10.1088/1755-1315/1085/1/012028

Bohnsack D, Potten M, Freitag S et al (2021) Stress sensitivity of porosity and permeability under varying hydrostatic stress conditions for different carbonate rock types of the geothermal Malm reservoir in Southern Germany. Geotherm Energy 9:15. https://doi.org/10.1186/s40517-021-00197-w

Chamorro CR, Mondéjar ME, Ramos R et al (2012) World geothermal power production status: energy, environmental and economic study of high enthalpy technologies. Energy 42:10–18. https://doi.org/10.1016/j.energy.2011.06.005

van Esch M, Bloemendal M, Hartog N, Vardon P (2025) Considerations for placement of ATES Triplet wells.

Cooper JR, Dooley RB (2007) Revised release on the IAPWS industrial formulation 1997 for the thermodynamic properties of water and steam. Int Assoc Prop Water Steam 1:48

Cröniger C, Tretter R, Eichenseer P, et al (2022) Approach to climate neutral heat supply in munich 2035. In: Proceedings of the European Geothermal Congress

Cui X, Wong LNY (2022) A 3D fully thermo–hydro–mechanical coupling model for saturated poroelastic medium. Comput Methods Appl Mech Eng 394:114939. https://doi.org/10.1016/j.cma.2022.114939

Dashti A, Gholami Korzani M, Geuzaine C et al (2023) Impact of structural uncertainty on tracer test design in faulted geothermal reservoirs. Geothermics 107:102607. https://doi.org/10.1016/j.geothermics.2022.102607

Dashti A, Grimmer JC, Geuzaine C et al (2024) Developing meshing workflows in Gmsh v4.11 for the geologic uncertainty assessment of high-temperature aquifer thermal energy storage. Geosci Model Dev 17:3467–3485. https://doi.org/10.5194/gmd-17-3467-2024

DeWolf S, Wyatt FK, Zumberge MA, Hatfield W (2015) Improved vertical optical fiber borehole strainmeter design for measuring Earth strain. Rev Sci Instrum 86:114502. https://doi.org/10.1063/1.4935923

Dickinson JS, Buik N, Matthews MC, Snijders A (2009) Aquifer thermal energy storage: theoretical and operational analysis. Geotechnique 59:249–260. https://doi.org/10.1680/geot.2009.59.3.249

Dobson P, McLing T, Spycher N et al (2025) High-temperature aquifer thermal energy storage (HT-ATES) projects in Germany and the Netherlands—review and lessons learned. Energies 18:6292. https://doi.org/10.3390/en18236292

Fadel M, Reinecker J, Bruss D, Moeck I (2022) Causes of a premature thermal breakthrough of a hydrothermal project in Germany. Geothermics 105:102523. https://doi.org/10.1016/j.geothermics.2022.102523

Fleuchaus P, Godschalk B, Stober I, Blum P (2018) Worldwide application of aquifer thermal energy storage – a review. Renew Sustain Energy Rev 94:861–876. https://doi.org/10.1016/j.rser.2018.06.057

Gan Q, Elsworth D (2014) Analysis of fluid injection-induced fault reactivation and seismic slip in geothermal reservoirs. J Geophys Res Solid Earth 119:3340–3353. https://doi.org/10.1002/2013JB010679

Potten M (2020) Geomechanical characterization of sedimentary and crystalline geothermal reservoirs

Geuzaine C, Remacle J (2009) Gmsh: a 3-D finite element mesh generator with built-in pre- and post-processing facilities. Int J Numer Methods Eng 79:1309–1331. https://doi.org/10.1002/nme.2579

Ghassemi A (2012) A review of some rock mechanics issues in geothermal reservoir development. Geotech Geol Eng 30:647–664. https://doi.org/10.1007/s10706-012-9508-3

Gholinia A, Nikkhah M, Naderi R (2022) Validation of borehole extensometers results in geotechnical monitoring. Environ Earth Sci 81:312. https://doi.org/10.1007/s12665-022-10422-9

Habibi R, Zare S, Asgari A et al (2023) Coupled thermo-hydro-mechanical-chemical processes in salt formations for storage applications. Renew Sustain Energy Rev 188:113812. https://doi.org/10.1016/j.rser.2023.113812

Hassan Q, Viktor P, Al-Musawi TJ, Ali BM, Algburi S, Alzoubi HM, Al-Jiboory AK, Sameen AZ, Salman HM, Jaszczur M (2024) The renewable energy role in the global energy Transformations Renew Energy. Focus 48:100545. https://doi.org/10.1016/j.ref.2024.100545

Heldt S, Wang B, Bauer S (2023) Parameter identification and range restriction through sensitivity analysis for a high-temperature heat injection test. Geotherm Energy 11:12. https://doi.org/10.1186/s40517-023-00255-5

Heldt S, Beyer C, Bauer S (2024) Uncertainty assessment of thermal recovery and subsurface temperature changes induced by high-temperature aquifer thermal energy storage (HT-ATES): a case study. Geothermics 122:103086. https://doi.org/10.1016/j.geothermics.2024.103086

Hörbrand T, Beichel K, Bendias D et al (2025) Karst control on reservoir performance of a developed carbonate geothermal reservoir in Munich, Germany. Geol Soc Lond Spec Publ 548:291–310. https://doi.org/10.1144/SP548-2024-42

Hörbrand T, Mayr M, Beichel K et al (2023) VESTA Malm – high temperature ATES in the Malm reservoir of the greater Munich region. Essen

Jacobson MZ, Delucchi MA, Bauer ZAF et al (2017) 100% clean and renewable wind, water, and sunlight all-sector energy roadmaps for 139 countries of the world. Joule 1:108–121. https://doi.org/10.1016/j.joule.2017.07.005

Jin W, Atkinson T, Neupane G, et al (2022) Influence of Mechanical Deformation and Mineral Dissolution/precipitation on Reservoir Thermal Energy Storage. In: 56th U.S. Rock Mechanics/Geomechanics Symposium. ARMA, Santa Fe, New Mexico, USA, p ARMA-2022–2068

Koh J, Roshan H, Rahman SS (2011) A numerical study on the long term thermo-poroelastic effects of cold water injection into naturally fractured geothermal reservoirs. Comput Geotech 38:669–682. https://doi.org/10.1016/j.compgeo.2011.03.007

Kong Y, Pang Z, Shao H, Kolditz O (2017) Optimization of well-doublet placement in geothermal reservoirs using numerical simulation and economic analysis. Environ Earth Sci 76:118. https://doi.org/10.1007/s12665-017-6404-4

Konrad F, Savvatis A, Degen D et al (2021) Productivity enhancement of geothermal wells through fault zones: efficient numerical evaluation of a parameter space for the Upper Jurassic aquifer of the North Alpine Foreland Basin. Geothermics 95:102119. https://doi.org/10.1016/j.geothermics.2021.102119

Lee KS (2010) A review on concepts, applications, and models of aquifer thermal energy storage systems. Energies 3:1320–1334. https://doi.org/10.3390/en3061320

Lei X, He S, Abed A et al (2021) A generalized interpolation material point method for modelling coupled thermo-hydro-mechanical problems. Comput Methods Appl Mech Eng 386:114080. https://doi.org/10.1016/j.cma.2021.114080

Li T, Shiozawa S, McClure MW (2016) Thermal breakthrough calculations to optimize design of a multiple-stage enhanced geothermal system. Geothermics 64:455–465. https://doi.org/10.1016/j.geothermics.2016.06.015

Lindsay AD, Gaston DR, Permann CJ et al (2022) 2.0 - MOOSE: enabling massively parallel multiphysics simulation. SoftwareX 20:101202. https://doi.org/10.1016/j.softx.2022.101202

Lindsey NJ, Rademacher H, Ajo-Franklin JB (2020) On the broadband instrument response of fiber-optic DAS arrays. J Geophys Res Solid Earth 125:e2019JB018145. https://doi.org/10.1029/2019JB018145

Mahon H, O'Connor D, Friedrich D, Hughes B (2022) A review of thermal energy storage technologies for seasonal loops. Energy 239:122207. https://doi.org/10.1016/j.energy.2021.122207

McTigue DF (1986) Thermoelastic response of fluid-saturated porous rock. J Geophys Res Solid Earth 91:9533–9542. https://doi.org/10.1029/JB091iB09p09533

Megies T, Wassermann J (2014) Microseismicity observed at a non-pressure-stimulated geothermal power plant. Geothermics 52:36–49. https://doi.org/10.1016/j.geothermics.2014.01.002

van der Baan M, Eaton D, Dusseault M (2013) Microseismic Monitoring Developments in Hydraulic Fracture Stimulation. OnePetro

Birdsell DT, Saar MO (2020) Modeling ground surface deformation at the swiss HEATSTORE underground thermal energy storage sites. In: World Geothermal Congress (WGC 2020+ 1). ETH Zurich, Institute of Geophysics, p 22046

Jahanbakhsh K, Nakagawa M, Arshad M, Dunnington L (2016) Modeling Thermal Breakthrough in Sedimentary Geothermal System, Using COMSOL Multiphysics

Moeck IS (2014) Catalog of geothermal play types based on geologic controls. Renew Sustain Energy Rev 37:867–882. https://doi.org/10.1016/j.rser.2014.05.032

Egert R, Gaucher E, Savvatis A, et al (2022) Numerical determination of long-term alterations of THM characteristics of a Malm geothermal reservoir during continuous exploitation

Pandey SN, Vishal V, Chaudhuri A (2018) Geothermal reservoir modeling in a coupled thermo-hydro-mechanical-chemical approach: a review. Earth-Sci Rev 185:1157–1169. https://doi.org/10.1016/j.earscirev.2018.09.004

Parisio F, Vilarrasa V, Wang W et al (2019) The risks of long-term re-injection in supercritical geothermal systems. Nat Commun 10:4391. https://doi.org/10.1038/s41467-019-12146-0

Quinn JJ, Tomasko D, Kuiper JA (2006) Modeling complex flow in a karst aquifer. Sediment Geol 184:343–351. https://doi.org/10.1016/j.sedgeo.2005.11.009

Reinecker J, Tingay M, Müller B, Heidbach O (2010) Present-day stress orientation in the Molasse Basin. Tectonophysics 482:129–138. https://doi.org/10.1016/j.tecto.2009.07.021

Mraz E (2019) Reservoir characterization to improve exploration concepts of the Upper Jurassic in the southern Bavarian Molasse Basin. Technische Universität München

Seithel R, Gaucher E, Mueller B et al (2019) Probability of fault reactivation in the Bavarian Molasse Basin. Geothermics 82:81–90. https://doi.org/10.1016/j.geothermics.2019.06.004

Shah M, Prajapati M, Yadav K, Sircar A (2024) A comprehensive review of geothermal energy storage: methods and applications. J Energy Storage 98:113019. https://doi.org/10.1016/j.est.2024.113019

Shapiro SA, Dinske C, Kummerow J (2007) Probability of a given-magnitude earthquake induced by a fluid injection. Geophys Res Lett 34:2007GL031615. https://doi.org/10.1029/2007GL031615

Shi H, Wang G, Lu C (2023) Numerical investigation on delaying thermal breakthrough by regulating reinjection fluid path in multi-aquifer geothermal system. Appl Therm Eng 221:119692. https://doi.org/10.1016/j.applthermaleng.2022.119692

Solangi YA, Magazzino C (2025) Evaluating financial implications of renewable energy for climate action and sustainable development goals. Renew Sustain Energy Rev 212:115390. https://doi.org/10.1016/j.rser.2025.115390

Stanchits S, Burghardt J, Surdi A (2015) Hydraulic fracturing of heterogeneous rock monitored by acoustic emission. Rock Mech Rock Eng 48:2513–2527. https://doi.org/10.1007/s00603-015-0848-1

Stober I, Jägle M, Kohl T (2023) Optimizing scenarios of a deep geothermal aquifer storage in the southern Upper Rhine Graben. Geotherm Energy 11:34. https://doi.org/10.1186/s40517-023-00275-1

Stricker K, Egert R, Schill E, Kohl T (2024) Risk of surface movements and reservoir deformation for high-temperature aquifer thermal energy storage (HT-ATES). Geotherm Energy 12:4. https://doi.org/10.1186/s40517-024-00283-9

Dashti A (2026) Thermo-hydro-mechanical impacts of the operation style in a faulted Malm reservoir: Storage Triplet vs. Hydrothermal Doublet

Vaezi I, Yoshioka K, De Simone S et al (2025) A review of thermo-hydro-mechanical modeling of coupled processes in fractured rock: from continuum to discontinuum perspective. J Rock Mech Geotech Eng 17:7460–7488. https://doi.org/10.1016/j.jrmge.2025.04.033

Wadas SH, Krumbholz JF, Shipilin V et al (2023) Advanced seismic characterization of a geothermal carbonate reservoir – insight into the structure and diagenesis of a reservoir in the German Molasse Basin. Solid Earth 14:871–908. https://doi.org/10.5194/se-14-871-2023

Wagner W, Pruß A (2002) The IAPWS formulation 1995 for the thermodynamic properties of ordinary water substance for general and scientific use. J Phys Chem Ref Data 31:387–535. https://doi.org/10.1063/1.1461829

Wang J, Tan X, Zhao Z et al (2024) Coupled thermo-hydro-mechanical modeling on geothermal doublet subject to seasonal exploitation and storage. Energy 293:130650. https://doi.org/10.1016/j.energy.2024.130650

Wesselink M, Liu W, Koornneef J, Van Den Broek M (2018) Conceptual market potential framework of high temperature aquifer thermal energy storage - A case study in the Netherlands. Energy 147:477–489. https://doi.org/10.1016/j.energy.2018.01.072

Wilkins A, Green CP, Ennis-King J (2021) An open-source multiphysics simulation code for coupled problems in porous media. Comput Geosci 154:104820. https://doi.org/10.1016/j.cageo.2021.104820

Wolfgramm M, Bartels J, Hoffmann F, et al (2007) Unterhaching geothermal well doublet: structural and hydrodynamic reservoir characteristic; Bavaria (Germany). In: European Geothermal Congress

Zareidarmiyan A, Salarirad H, Vilarrasa V et al (2020) Comparison of numerical codes for coupled thermo-hydro-mechanical simulations of fractured media. J Rock Mech Geotech Eng 12:850–865. https://doi.org/10.1016/j.jrmge.2019.12.016

Zhang S, Shi Z, Wang G (2019) Comparison of aquifer parameters inferred from water level changes induced by slug test, earth tide and earthquake – a case study in the three Gorges area. J Hydrol 579:124169. https://doi.org/10.1016/j.jhydrol.2019.124169

Zhou XX, Ghassemi A, Cheng AH-D (2009) A three-dimensional integral equation model for calculating poro- and thermoelastic stresses induced by cold water injection into a geothermal reservoir. Int J Numer Anal Methods Geomech 33:1613–1640. https://doi.org/10.1002/nag.780

Ziegler MO, Heidbach O (2020) The 3D stress state from geomechanical–numerical modelling and its uncertainties: a case study in the Bavarian Molasse Basin. Geotherm Energy 8:11. https://doi.org/10.1186/s40517-020-00162-z

Zoback MD (2007) Reservoir geomechanics, 1st edn. Cambridge University Press

Bruss D, Barenth F, Greller M, et al (2018) Verbundvorhaben: Ganzheitlich optimierte und nachhaltige Reservoirerschließung für tiefengeothermische Anlagen im bayerischen Molassebecken; Teilvorhaben: Entwicklung eines 50 MWel Kraftwerks und Erschließung von 400 MWth für die Fernwärme in München : Endbericht : Laufzeit des Vorhabens: 01.12.2014–31.03.2018, verlängert bis 31.09.2018. SWM Services GmbH. URL https://www.tib.eu/suchen/id/TIBKAT:1677566647/